

8599

APPLICATION OF ION IMPLANTATION TECHNIQUES TO ANODE ELECTROCATALYST^A
DEVELOPMENT FOR USE IN ALKALINE WATER ELECTROLYSIS

APPLICATION OF ION IMPLANTATION TECHNIQUES TO ANODE ELECTROCATALYST
DEVELOPMENT FOR USE IN ALKALINE WATER ELECTROLYSIS

by

USMAN GBADEBO AKANO, B.Sc. (Ife)

A Report

Submitted to the School of Graduate Studies
in Partial Fulfilment of the Requirements for
the Degree
Master of Engineering

PART B

McMaster University
1980

MASTER OF ENGINEERING 1980
Department of Engineering Physics

McMASTER UNIVERSITY
Hamilton, Ontario

TITLE: Application of Ion Implantation Techniques to Anode Electro-
catalyst Development for Use in Alkaline Water Electrolysis

AUTHOR: Usman Gbadebo Akano, B.Sc. (Ife)

SUPERVISOR: Dr. D.A. Thompson

NUMBER OF PAGES: vii, 88

TABLE OF CONTENTS

	<u>Page</u>
ABSTRACT	iii
ACKNOWLEDGEMENT	iv
LIST OF TABLES	v
LIST OF FIGURES	vi
CHAPTER 1 - INTRODUCTION	1
CHAPTER 2 - ION BOMBARDMENT OF SURFACES	4
2.1 Ion Implantation	4
2.2 Recoil Implantation	11
2.3 Application of Ion Implantation to Metals	14
2.4 Analysis Technique	17
CHAPTER 3 - EXPERIMENTAL	23
CHAPTER 4 - RESULTS AND DISCUSSION	26
4.1 Uniformly Distributed Implants	26
4.2 Li-Implanted Ni Electrodes	28
4.3 Li Implanted NiO Electrode	28
4.4 Ag-implanted Ni Electrode	30
4.5 Recoil Implanted Ag in Ni, NiO	32
4.6 Kr ⁺ Ion Implanted Ni Electrode	33
4.7 Overpotential and Kinetic Parameters of the Test Electrodes	33
4.6.1 Electrode Potential	33
4.6.2 Kinetic Parameters	35
4.8 RBS Analysis from Ag-implanted Electrode	36
CHAPTER 5 - CONCLUSIONS	39
CHAPTER 6 - SUGGESTIONS FOR FURTHER WORK	41
REFERENCES	87

ABSTRACT

The project is concerned with development of suitable anode electrodes for oxygen evolution in 30 w/o KOH solution at 80°C. Li ions (15 keV, 40 keV and 60 keV) at doses of 1×10^{15} to 1.5×10^{16} ions/cm², He ions (15 keV, 40 keV) at 3×10^{15} ions/cm² and Ag ion (50 keV) at 1×10^{16} to 4×10^{16} ions/cm² have been implanted into polycrystalline Ni and oxidized Ni at room temperature. Ag has also been recoil implanted into Ni and NiO. Current-potential measurements have been carried out using galvanostatic techniques with the implanted samples as the oxygen electrode in 30 w/o KOH solution at 80°C. The Ag-implanted electrodes show a substantial reduction in electrode potential at 1 A/cm² (~ 60% compared to polished Ni) and all implanted samples show a more uniform corrosion products on the surface. Dual Tafel slopes are observed for all electrodes and the higher slope at the higher current densities is thought to be due to the formation of nickel oxide on the electrodes. The Tafel slope and exchange current density, at low current densities are considered consistent with reported data.

RBS analysis of the Ag-implanted electrodes indicates that no Ag is lost as a result of the electrochemical measurements.

ACKNOWLEDGEMENT

The author would like to express sincere thanks to Dr. D.A. Thompson, first for suggesting this work, and second for his tutorage and constant advice. I also wish to thank Dr. W.W. Smeltzer, Dr. J.A. Davies and Dr. I. Tashlykov for all the illuminating discussions we had together. Dr. W.W. Smeltzer has contributed to ideas incorporated in the electrochemistry aspect of this work. For this I am very grateful. The Ag implantations were carried out by Dr. Davies at Chalk River Nuclear labotatories and for this I am very grateful. Financial support of the University of Ife and McMaster University are deeply appreciated.

LIST OF TABLES

- Table 1: Measured electrode potential on test electrodes for oxygen evolution in 30 w/o KOH at 80°C.
- Table 2: Kinetic parameters for oxygen evolution on test electrodes for galvanostatic sweep from 0.1 to 150 mA/cm².
- Table 3: Kinetic parameters for oxygen evolution on Ni, and implanted Ni electrodes. Current sweep from 0.1 - 1,500 mA/cm².

LIST OF FIGURES

- Fig. 1: Rate of ion energy loss (nuclear).
- Fig. 2: Rate of ion energy loss (electronic).
- Fig. 3: Illustration of recoil implantation.
- Fig. 4: Distribution of recoil-implanted atoms.
- Fig. 5: Backscattering geometry and principle of elastic scattering (after Bøgh 1968).
- Fig. 6: Ion implantation facility.
- Fig. 7: Target chamber schematics.
- Fig. 8: Uniformly distributed Li⁺ implants in Ni.
- Fig. 9: Uniformly distributed He⁺ implants in Ni.
- Fig. 10: SEM examination of Ni surface implanted with $\sim 1 \times 10^{15}$ Li⁺ ions/cm².
- Fig. 11: Ni surface (SEM) after $\sim 3 \times 10^{15}$ He⁺ ions/cm².
- Fig. 12: Current-potential curves for Li and He implanted Ni electrode - low current density.
- Fig. 13: I-V curve for Li and He implanted Ni electrode - high current density.
- Fig. 14: Microscopic nature of the Ni electrode surface.
(a) before implant,
(b) He implanted and unimplanted,
(c) Unimplanted and Li (1×10^{15} ions/cm²) implants.
- Fig. 15: I-V relations for 1.1×10^{16} Li ions/cm² implanted Ni electrode:

- (a) Low current densities,
- (b) High current densities.

Fig. 16: Optical micrograph of the Li-implanted electrode taken after polarization measurements.

Fig. 17(a&b): I-V curve for Li implanted NiO electrodes.

Fig. 18(a&b): I-V curve for 1×10^{16} Ag ions/cm² implanted Ni electrode.

Fig. 19(a&b): I-V curve for 4×10^{16} Ag⁺ ions/cm² implanted Ni electrode.

Fig. 20(a&b): Optical micrograph of the Ag-implanted electrode after polarisation.

Fig. 20(c): RBS spectra of Ag-implanted samples.

Fig. 21,22: I-V curve for Ni electrode with Ag recoil-implanted Ni and NiO.

Fig. 23: I-V curve for Kr-implanted electrode.

Fig. 24: RBS of recoil-implanted Ni.

Fig. 25: RBS of recoil implanted NiO.

Fig. 26(a-d): Overpotential versus log of current density for test electrodes.

CHAPTER 1
INTRODUCTION

The traditional oxygen electrode material is nickel or nickel-coated steel because it has one of the lowest overpotentials for oxygen evolution reaction of all non-noble metals, and because of its high resistance to corrosion in hot concentrated caustic solution. However it becomes necessary to develop electrocatalysts which have higher activity than nickel if the objective (desired) of 100% energy efficiency is to be achieved or even approached.

Improved electrode activity has been achieved by operating the cell at higher temperatures,^{1,2} alloying of electrode with materials having high conductivity³ like lithium and using materials having high surface area.⁴ Other authors^{1, 5, 6, 7} have investigated materials having high potentials for electrocatalytic activity. In general most materials found suitable to improve electrocatalytic activity - Li, Ru, RuO₂, Ag and Pt — are all either scarce or expensive materials. As shown by Tseung et al.,⁴ and by Bevan⁸ an incorporation of 10 atom-% Li in Ni results in a six-fold increase in electrode performance. Bevan and Tseung also observed that 10 atom-% Li in NiO improves the conductivity at 25°C from 10⁻⁸ ohm⁻¹ cm⁻¹ to 1 ohm⁻¹ cm⁻¹ - a factor of 10⁸. The conclusion here is that only minute quantities of these materials need be incorporated in Ni in order to improve its electrochemical activity - a fortunate development in view of the cost and scarcity of these materials.

In the search for new electrocatalysts most authors have concentrated on the testing of new materials, bulk alloying with beneficial materials and oxide formation by heating in air: Li_2O incorporation into NiO surface layer, and titanium electrode activated by the noble metal oxide RuO_2 have involved immersion of the electrode in $\text{Li}(\text{OH})_2^9$ or in RuCl_4^7 followed by heating or thermal oxidation in air. These experimental methods are presently not well controlled plus the fact that they result in high consumption of the expensive metals. The ion implantation technique is very useful in this regard because desired materials can be incorporated in precise amounts, and their locations from the surface can be well controlled. Since ion implantation is a non-equilibrium process, no solubility limits are involved thus alloys of varying composition are possible - an advantage in electrocatalysis since catalytic activity changes with composition.

There are only a few publications in the literature concerning application of ion implantation to produce better electrocatalysts. Grenness et al.¹⁰ have observed significant effects on the rate of hydrogen evolution after introduction of minute quantities of Pt into tungsten and tungstic oxide. Rabette et al.³ have also implanted Pt into monocrystalline supports of $\alpha\text{-Al}_2\text{O}_3$ and MgO and concluded that the nature of pretreatment has a profound effect on the catalytic activity. Dearnaley¹¹ and his group at Harwell have long used ion implantation technique to improve corrosion resistance.

In this report we have directly implanted Ni and NiO with various species - Li (at 15, 40, 60 keV), He (at 20-, 40- keV),

Ag at 50 keV. Also we have attempted recoil implantation of Ag and Pt into Ni.

Chapter 2 describes ion implantation of surfaces and 2.2 describes recoil implantation, while section 2.3 describes application of ion implantation to metals. Section 2.4 describes the Rutherford Backscattering analysis technique. Chapter 3 details the experimental facilities, and the experiments including electrochemical measurements on the implanted electrodes. In Chapter 4 we discuss the experimental results while Chapter 5 gives the conclusions and some suggestions for further work are given in Chapter 6.

CHAPTER 2
ION BOMBARDMENT OF SURFACES

2.1 Ion Implantation

Ion implantation is a technique for the incorporation of foreign atoms into a substrate called the target. The foreign species can be atoms or molecules, and the word "ion" underlies the fact that the atoms (or molecules) to be implanted are ionized. Thus the species to be implanted are first ionized in an ion source to form a beam of ions. The beam of ions is focussed and then accelerated by an electric field and mass analyzed by electromagnetic means to hit a suitable target sitting in vacuum in a target chamber. Usual implantation energies range from ~ 10 keV to several hundreds of keV.

When moving ions impinge on the target, physical processes result in damage and property changes of a thin surface layer of the target. The atoms will slow down in the target as a result of collisions with target atoms and electrons in the solid. These elastic and in-elastic (ionization) interaction processes will eventually bring the atoms to rest in the target. As the implantation progresses a concentration distribution for the implanted species with depth develops and the distribution is approximately Gaussian

about a mean range.¹¹ The distribution depends mainly on the mass ratio M_1/M_2 , - M_1 is the mass of the ion and M_2 the mass of the target - Z_1 (the atomic number of the ion) and the kinetic energy, E .

Lindhard¹² considered the two main processes of energy loss by ions traversing a solid - the electronic and nuclear processes - as independent, and that both processes contribute to the overall rate of energy loss, i.e.

$$\left(-\frac{dE}{dx}\right)_{\text{total}} = \left(-\frac{dE}{dx}\right)_e + \left(-\frac{dE}{dx}\right)_n \quad (1)$$

where

$\left(-\frac{dE}{dx}\right)_e$ is the rate of energy loss due to electronic excitation and ionization, and

$\left(-\frac{dE}{dx}\right)_n$ is the rate of energy loss due to elastic collisions between the impinging ions and the atoms of the target.

In 1963 the "LSS" Theory based on the work of Lindhard and Scharff,³⁸ emerged to describe the rate of energy loss of energetic ions in amorphous solids. An interaction potential between the ion and target atom was assumed to be screened-coulomb potential of the Thomas-Fermi type:

$$V(\gamma) = \frac{Z_1 Z_2 e^2}{\gamma} \phi\left(\frac{\gamma}{a}\right) \quad (2)$$

where Z_1 , Z_2 are the atomic numbers of the ion and target atom respectively, γ is the separation distance, e is electronic charge and a is the Thomas-Fermi screening length given as

$$a = 0.885 a_0 (Z_1^{2/3} + Z_2^{2/3})^{-1/2}$$

where

$$a_0 \equiv \text{Bohr radius } (= 0.529 \text{ \AA})$$

$\phi(\gamma/a) \equiv$ Thomas-Fermi screening function and is tabulated by Gombas.

In the process of nuclear stopping, the implanted atoms lose energy by collision with the target atoms. The energy transferred to the target atom is

$$E_2 = \frac{4 M_1 M_2}{(M_1 + M_2)^2} E_1 \sin^2 \frac{\phi}{2} \quad (3)$$

where

$E_1 =$ projectile energy, and

$\phi =$ scattering angle in the C of M system.

Thus the maximum energy is transferred for head-on collision ($\phi = 180^\circ$) and this energy is

$$E_m = \frac{4 M_1 M_2}{(M_1 + M_2)^2} E_1 \quad (4)$$

The nuclear stopping or the rate of energy loss due to an elastic collision is

$$\left(-\frac{dE}{dx}\right)_n = N \int_0^{E_m} E_2 \left(\frac{d\sigma_n}{dE_2}\right) dE_2 \quad (5)$$

where

$$\frac{d\sigma_n}{dE_2}$$

is the differential scattering cross-section. The rate of

electronic energy loss is given³⁸ as

$$\left(-\frac{dE}{dx}\right)_e = \frac{8 Z_1^{1/6}}{0.885} \left(\frac{Z_1 Z_2 e^2}{a}\right) a^2 N \left(\frac{V}{V_0 (Z_1^{2/3} + Z_2^{2/3})}\right) \quad (6)$$

where

V = velocity of the ion

V_0 = Bohr velocity ($= c/137$) $\frac{e^2}{h}$

N = number of atoms per unit volume in the target.

Equation (6) can be expressed in terms of the dimensionless energy parameter ϵ (corresponding to a projectile energy of $E = 1$ keV), and the dimensionless range parameter ρ (corresponding to a projectile range X of $1 \mu\text{g cm}^{-2}$ in the target)¹³ where

$$\epsilon = \frac{E \cdot a M_2}{Z_1 Z_2 e^2 (M_1 + M_2)} \quad (7)$$

and

$$\rho = \frac{X M_2 N \cdot 4\pi a^2}{(M_1 + M_2)^2} \quad (8)$$

Therefore the electronic energy loss rate becomes

$$\left(\frac{dE}{dp}\right)_e = K \epsilon^{1/2} \quad (9)$$

with

$$K = \xi_e \frac{0.079 Z_1^{1/2} Z_2^{1/2} \cdot (A_1 + A_2)^{3/2}}{(Z_1^{2/3} + Z_2^{2/3})^{3/4} A_1^{3/4} \cdot A_2^{1/2}} \quad (10)$$

$$\xi_e = Z_1^{1/6}$$

For most ion-solid interactions the value of K lies between 0.1 and 1.5. Figure 2 shows the variation of $(\frac{dE}{d\rho})_e$ for $k = 0.15$ and 1.5. A plot of $(\frac{dE}{d\rho})_n$, the nuclear stopping, as a function of energy is also shown in Fig. 1. Figures 1 and 2 thus indicate that nuclear stopping dominates at lower energies while the electronic stopping is dominant at higher energies.

Range and Spatial Distribution of Ions

The average total path length, R_T , of the ion in the solid is

$$R_T(E) = \int_0^E \frac{dE}{\left(-\frac{dE}{dx}\right)_n + \left(-\frac{dE}{dx}\right)_e} \quad (11)$$

One can use the Transport Equation to derive the range distribution of particles in a target.

If

$P(E,R)dR$ = probability that a particle with energy E will stop between R and $R + dR$

then

$$\int_0^{\infty} P(E,R)dR = 1$$

$$\langle R^n \rangle = \int_0^{\infty} R^n P(E,R)dR \text{ is called the } n^{\text{th}} \text{ moment.}$$

We recall that the scattering cross-section probability

$$P(\psi)d\psi = N \cdot \Delta x d\sigma$$

We can then write a balance condition for the number of particles before and after collision:

$$P(E,R) = N \cdot dR \int_{T=E}^{T=E_m} d \cdot P(E-T, R-dR) + (1-NdR \int_E^{E_m} d\sigma) \times P(E, R-dR)$$

where E is the minimum energy transferred. Integrating the L.H.S. by parts and using the first, 2nd, 3rd and 4th moments, $\langle R \rangle$, $\langle R^2 \rangle$, $\langle R^3 \rangle$ and $\langle R^4 \rangle$ respectively and $\langle R^2 \rangle = \langle (R - \Delta R)^2 \rangle$ etc. to construct particle distribution assuming statistical distribution we have

$$N(R) P(E,R)dR \approx \frac{dR.N}{\sqrt{2\pi} \langle \Delta R^2 \rangle^{1/2}} \exp \left\{ - \frac{(R - \langle R \rangle)^2}{2 \langle \Delta R^2 \rangle} \right\}$$

which is the Gaussian approximation.

$\langle R \rangle$ = most probable range

$\langle \Delta R^2 \rangle^{1/2}$ = range straggling.

The depth of the peak of the distribution, like the overall distribution depends on ion energy and M_1/M_2 ratio. If M_1/M_2 is low ($\ll 1$), the peak concentration is close to the surface.

The above comments about the distribution are true only for completely amorphous targets and infinite medium. In a crystalline target the channeling effect may be important. The channelling effect is the process whereby all ions incident along (or sufficiently close to) a major crystallographic axis or plane are steered by a series of gentle collisions. Lindhard shows that above a certain critical angle of incidence to the atom row or plane, the atom cannot be channelled.

This critical angle is

$$\psi_c = k \left\{ \frac{2 Z_1 Z_2 e^2}{Ed} \phi \left(\frac{1.2 x_{rms}}{a} \right) \right\}^{1/2} \quad (12)$$

where x_{rms} is the mean square amplitude of vibration of the atom in the row. The effect of channeling is that the implanted atoms are able to penetrate deeper into the target before coming to rest. In such cases, the ion ranges and distribution will differ from those

predicted by the amorphous model.

Another factor that may affect ion distribution is radiation enhanced diffusion. If the implanted atoms can easily diffuse through the target, their range and distribution in the target will be different from predictions based on collision theory alone. Diffusion effect becomes important if implanted species are annealed at high temperature or if the beam current is sufficiently high to substantially raise the target temperature. Also radiation-enhanced diffusion due to mobile point defects accelerates normal diffusion.

For the high energy region where electronic stopping is dominant, it has been found that the electronic energy loss rate does not exhibit the monotonic Z_1 dependence given by LSS theory. An oscillatory dependence on Z_1 is observed¹⁴ which will cause departures from the theoretical ranges. This effect, theoretically treated by Firsov¹⁵ and Cheshire et al.,¹⁶ is attributed to the shell structure of the moving atom - the atoms of smaller size having lower electronic energy loss rates.

Another process that affects the distribution and concentration of implanted species at the surface of the target is sputtering. Sputtering is the gradual erosion of a target's surface due to ion bombardment. During ion bombardment sufficient energy may be transferred to the surface atoms so that they can escape from the target surface. The effect of this is that peak concentration position moves towards the surface.

2.2 Recoil Implantation

Recoil implantation is the introduction of impurity atoms into a substrate by atomic recoil of atoms sitting on a target. In deliberate recoil implantation a thin layer of the material to be recoil implanted is evaporated on to a substrate (into which the implant is desired), Fig. 3. The evaporated layer and the substrate then form a composite target. The target is then bombarded with energetic ions - usually inert gas ions like Ar or Kr. In the "thin" film treatment, film thickness, bombarding ion and its energy is normally chosen so that the bombarding ion has a range greater than the film thickness. If the energy transferred to an atom in the evaporated film is greater than $E_d \sim 25$ eV (the energy required to successfully displace an atom from its lattice position) the atom is likely to be displaced from its original position thus creating a vacancy - interstitial pair (or point defects). If the energy transferred is $\gg 25$ eV, the primary displaced atom may in turn displace other atoms within the layer thus giving rise to collision cascades.

Recoil implantation can be viewed as a form of "forward sputtering" while the opposite effect, the erosion of a target surface, can be viewed as "backward sputtering". In the process of recoil implantation erosion of the evaporated layer due to sputtering is going on as well and is in fact more rapid than the rate of recoil implantation since the sputtering ratio - the number of atoms ejected from the surface per incident ion (for most ion-target combinations) is greater than unity whereas the recoil yield is often

less than that. The implication is that the recoiled layers are being removed by sputtering as fast as they are formed unless the starting evaporated film is sufficiently thick.

Nelson¹⁷ has developed a theory of recoil implantation for "thin" targets using the concept of energy density within collision cascades. The flux of recoils crossing any plane surface with energy E in dE initiated by a primary recoil spectrum $W(E_\gamma)dE_\gamma$ is

$$\psi(E, E_1) \approx \frac{d}{E^2} \int_E^{\hat{E}_\gamma} W(E_\gamma) E_\gamma dE_\gamma \quad (13)$$

where

E_1 is energy of incident particle

E_γ is energy transferred to a recoil

\hat{E}_γ is maximum energy transferrable

$$= \frac{4 M_1 M_2}{(M_1 + M_2)^2}$$

d is the mean inter-atomic spacing.

For heavy particles, the differential scattering cross-section, $d\sigma$, is isotropic and can be approximated by the expression

$$d\sigma(E_\gamma, E_1) = \frac{\sigma(E_1) dE_\gamma}{\hat{E}_\gamma} \quad (14)$$

The fundamental assumption of Nelson is to use a simple inverse square interaction potential in order to obtain the total cross-section $\sigma(E_1)$ and obtained

$$\sigma(E_1) = \frac{2\pi a_0^2 E_R Z_1 Z_2 (M_1 + M_2)}{(\exp 1) M_2 (Z_1^{2/3} + Z_2^{2/3})^{1/2} E_1} \quad (15)$$

E_R = Rydberg energy. The recoil spectrum then becomes

$$W(E_\gamma)dE_\gamma = N_0 \phi d\sigma(E_\gamma, E_1) \quad (16)$$

N_0 = atomic density

ϕ \equiv flux of bombarding particle.

Thus Nelson obtained an expression for the flux of recoils as

$$\psi(E, E_1) = \frac{4\pi a_0^2 d N_0 \phi E_R \cdot Z_1 Z_2 M_1}{\exp(1)(M_1 + M_2)(Z_1^{2/3} + Z_2^{2/3})^{1/2}} \cdot \left(\frac{1}{E^2} - \frac{1}{\hat{E}_\gamma^2} \right) \quad (17)$$

If the maximum energy transferrable $\hat{E}_\gamma \gg E$, then $\psi \propto \frac{1}{E^2}$. If $E \leq \hat{E}_\gamma$, then the flux falls off more rapidly than a $1/E^2$ dependence. The total number of recoils is obtained by integrating over a minimum energy (threshold for passing from the evaporated layer into the substrate) to the maximum transferrable energy.

Compared with direct implantation, there is a significant difference in the distribution of recoil-implanted and directly implanted species. Direct implant has a distribution that is approximately Gaussian with a reduced concentration at the surface. The distribution of recoil implants on the other hand shows (Fig. 4) that most of the recoils are right on the surface of the substrate and penetrating only to a few angstroms at moderate ion fluences. Thus if implants to a considerable depth ($\geq 100 \text{ \AA}$) is desired, direct ion implantation must be used. Recoil implantation is very useful in such cases when very high surface concentrations and shallow depths are desired. Also, in some cases it is very difficult if not impossible using an available ion source to produce certain ions e.g. Ru. In such cases recoil implantation may be useful.

Electrocatalytic behaviour is essentially a surface effect. Therefore the process of recoil implantation should prove useful in catalysis development.

2.3 Application of Ion Implantation to Metals

The widest application of ion implantation techniques to date has been in the field of semiconductor technology. The use of this technique to change electrical properties is detailed in the book by Mayer, Erickson and Davies and in many reviews.^{18,19} In these applications ion implantation is almost always combined with the channelling effect and RBS analysis. A number of property changes that occur in metals as a result of ion implantation, and their applications are also documented by Ziegler²⁰ and Dearnaley.^{11,21} In general these property changes fall into the following:

1. Electrochemical and chemical properties of metals.
2. Corrosion resistance.
3. Hardness, friction and wear properties.
4. Electrical resistivity.
5. Superconductivity.
6. Simulation of neutron radiation damage.
7. Implantation metallurgy.

In many cases only minute quantities of certain beneficial atoms are required to effect changes in both electrochemical and chemical properties of materials. Ion implantation technique can therefore afford a cheaper way of changing these properties compared to the

normal metallurgical process.

Many publications exist about the influence of ion implantation on the oxidation of some materials. Goode²² studied the influence of ion implantation on the oxidation of polycrystalline nickel for a range of implanted species, and found that the ions He⁺, Li⁺, Ne⁺, N⁺, and Xe⁺ all enhance oxidation to a degree which increases monotonically with mass number for implanted samples annealed at 370°C (which is less than the oxidation temperature of 630°C). However when the implanted samples were annealed before oxidation they found that the oxide ratio rise from 0.2 gradually with temperature reaching a peak at ~ 400°C and then decreases to a minimum (at ~550°C) and then begins to rise gradually. They therefore suggest that corrosion of Ni is controlled by physical factors of radiation damage and atomic radius of implanted species. Significantly, they did not observe any correlation of the oxidation with either electronegativity or valence.

Dearnaley et al.^{23,24} have investigated the thermal oxidation of titanium, stainless steel, zirconium and copper after implantation of various ions to depth of ~ 0.1 μm . They observed both enhancement and reduction in the oxidation rate. Implantation of the less-electronegative atoms (calcium, europium) reduced the rate of oxidation of titanium, whereas implants of the more electronegative species (Bi, In, Al) lowered the rate of oxidation of stainless steel. Implantation of Ar (an inert atom) was not found to have any effect on oxidation rate. Dearnaley et al. therefore concluded, in contrast to the observation of Goode, that radiation damage effect has no significant effect on the rate of oxidation. Naguib et al.²⁵ also investigated the influence of B, C, N, and Ne ions on the oxidation rate of Cu.

Their observation is that a high dose of B⁺ (10^{16} - 10^{17} ions/cm²) was very effective in reducing the rate of oxidation whereas both Ne and N were not so effective, and that C in fact increased the oxidation rate. Their conclusion is that the radiation damage in Cu following the bombardments is detrimental to the beneficial effects resulting from chemical doping of the implants - again in contrast to the conclusions of Dearnaley et al.²³.

Sood and Dearnaley²⁶ have formed metastable alloys of Ta, Sn and Er at room temperature in Ni by ion implantation. They found that Er, Ta and Sn have solubilities that are well beyond those expected under condition of thermal equilibrium.

Solid solubility (atom %)

$$= \frac{F}{\sqrt{2\pi}\Delta R_p} \cdot \frac{N_r}{N_h} \times 100 \quad (18)$$

where F is the substitutional fraction of an implanted species.

N_h is the concentration of host material (atom cm⁻³), N_r dose retained by the implanted specimen.

Sood and Dearnaley therefore concluded that a metastable substitutional alloy (with $F \geq 0.05$) will be formed if the ion-target combination satisfies two conditions:

1. The implanted species must have atomic radius that is within -15% to +40% of the host radius.

2. The electronegativity of the implant must be within ± 0.7 of that of the host atoms.

Concerning electrochemical effects Grenness et al. have reported dramatic effects on the electrocatalytic activity of tungsten and tungstic oxide implanted with $10^{15} - 10^{16}$ ions/cm² of platinum when used as cathode in the electrolysis of water. They reported the activity of the electrodes approached that of pure platinum itself.

In a review by Grant²⁷ many implanted species have been reported to reduce the rate of corrosion when the implanted samples are used as electrodes in aqueous and alkaline solutions. Platinum-implanted Ti electrode is reported to readily form Pt oxide followed by Cl₂ evolution at higher potentials in 10⁻² M HCl solution. This catalytic behaviour is observed immediately following implantation and requires no activation steps in contrast to the observations of Grenness et al. with platinum-implanted tungsten and tungstic oxide.

2.4 Analysis Technique

Rutherford Backscattering (RBS) Technique

The sample to be analysed is exposed to a monoenergetic beam of light ions, usually helium or protons at typical energies of 1-2 MeV. When the beam strikes the target, the particles in the beam will be scattered to reach a solid-state detector suitably placed from the target. For every ion incident on the detector, a voltage pulse is produced which will be proportional to the energy with which the ion reaches the detector. The energy of the scattered particle after the collision depends on the mass of the struck atom. Further the number of scattered particles reaching

the detector depends on the number of scattering centres or the substrate atom present. Therefore by observing the energy of the backscattered particles, the identity and concentration of atoms in the solid can be determined.

If E_0 is the energy of the incident particle, then its energy after being scattered from the surface is

$$E = K^2 E_0$$

where K (kinematic factor) is given by

$$K = \left[\frac{M_1 \cos\theta + (M_2^2 - M_1^2 \sin^2\theta)^{1/2}}{M_1 + M_2} \right]$$

M_1 is mass of projectile

M_2 is mass of target and

θ is the scattering angle in the LAB system.

If the ion is not scattered right at the surface, it will penetrate the target losing energy in the process. If its incident energy is E_0 then it will reach the detector with an energy E' given by

$$E' = K^2 \left[E_0 - \int_0^{X_1} S_1 dx \right] - \int_0^{X_2} S_2 dx$$

where S_1 is the mean value of the stopping power for the inward path and S_2 is that for the outward path. S_1 and S_2 are functions of energy X_1 , X_2 are the in-coming and out-going trajectories

$$X_1 = \frac{x}{\cos \theta_1}, \quad X_2 = \frac{x}{\cos \theta_2}$$

with x the depth of penetration before the particle is scattered.

The principle of elastic scattering is shown in Fig. 5.

The number of particles P scattered by atoms of mass M_2 into the solid angle ω is given⁵⁵ as

$$P = nN\Delta x\omega \sigma(E_0, \phi, M_1, Z_1, M_2, Z_2) \quad (22)$$

where

n = number of incident ions

N = number of scattering centres of mass M_2 per unit Vol

Δx = target thickness in cm.

Thus for thin target layers, the area under the impurity peak is proportional to the number of substrate atoms in the specimen.

The probability for scattering into the solid angle $d\omega$ is given by the Rutherford scattering formula:

$$\frac{d\sigma}{d\omega} = 1.3 \times 10^{-27} \left(\frac{Z_1 Z_2}{E_0}\right)^2 \cdot \left(\frac{M_1 + M_2}{M_2}\right)^2 \cdot \frac{1}{\sin^4 \phi/2} \text{ cm}^2/\text{sr} \quad (23)$$

From this equation one sees that

1. The higher the atomic number of the target Z_2 , the more is the number of counts per unit time from it.
2. Small scattering angles are favoured,
3. For particles scattered at some depth from the surface, its energy is less than E_0 and the scattering cross-section is increased somewhat, $\frac{d\sigma}{d\omega} \propto 1/E_0^2$.

If the target contains an impurity element whose mass M is

less than that of the target (M_2) the signal from it will be superimposed on that of the target. RBS is not a very useful technique for such cases. Also if $M_2 \ll M_1$ no backscattering from the target will take place.

The RBS technique can be used to perform depth analysis by relating the energy loss of backscattered particles to the stopping power of the target. The energy "seen" by target atoms deeper inside is diminished from the incident energy by an amount which is proportional to the stopping power of the target material. The stopping power for many target atoms have been tabulated by Ziegler and Chu.²⁸

From Eq. (21), if we consider the small depth ($\sim 1 \mu\text{m}$) over which the stopping power is constant then

$$E' = K^2 E_0 - x \left[K^2 S(E_0) + S(E') \frac{\cos \theta_1}{\cos \theta_2} \right] \quad (24)$$

giving

$$x = \frac{K^2 E_0 - E'}{\left[S(E_0) K^2 + S(E') \frac{\cos \theta_1}{\cos \theta_2} \right]} \quad (25)$$

where θ_1 is the angle the incoming beam makes with the normal to the target surface, θ_2 is that made by the out-going beam to the surface. The horizontal scale is therefore both a mass and depth scale with depth increasing to the left and mass to the right.

Frequently the energy loss per unit length (dE/dx) is used to express the stopping power of a medium. Chu et al. employed the concept of the number of atoms per square centimetre traversed by the implanting beam to express the stopping cross-section β :

$$\beta = \frac{1}{N} \frac{dE}{dx} \quad (26)$$

$$= \frac{M}{\rho N_0} \cdot \frac{dE}{dx} \quad (27)$$

where

ρ = mass density of the target

N_0 = Avogadro number

M = mass of target (atomic)

For compounds stopping cross-sections are simply additive e.g.

$$\beta_{\text{Fe}_3\text{O}_4} = 3\beta_{\text{Fe}} + 4\beta_{\text{O}} \quad (28)$$

For bombardments carried out in the energy regime where the Rutherford scattering law is valid (eq. 23), the number of counts n_i observed in an impurity peak (see Fig. 5) is related to the number of impurity atoms/cm², N_i , of surface as follows²⁹

$$n_i = f \cdot Z_i^2 N_i \cdot (it) \quad (29)$$

where Z_i is the atomic number of the impurity, (it) is the integrated beam current and f is a constant which depends on the scattered angle, detector geometry, and the energy and atomic number of the projectile.

In a similar manner the number of counts n_s , in one channel of the substrate spectrum (measured just below the surface) is related to the number of atoms of the substrate, N_s , contributing to that channel

$$n_s = f Z_s^2 N_s \cdot (it) \quad (30)$$

From equations (29) and (30)

$$\frac{n_i}{n_s} = \frac{Z_i^2}{Z_s^2} \cdot \frac{N_i}{N_s}$$

giving the number of impurity atoms/cm² as

$$N_i = \frac{n_i}{n_s} \left(\frac{Z_s}{Z_i} \right)^2 N_s \quad (31)$$

The n_i/n_s ratio is obtained directly from the observed energy spectrum. For good accuracy dead-time and background corrections are usually applied in the evaluation of the n_i/n_s ratio. The number of substrate atoms contributing to a given channel are calculated from the rate of energy loss, dE/dx in the substrate.

Usually 1-2 MeV He ions are used as the projectile. In this energy regime, the Rutherford scattering laws are well obeyed. Also the choice of He ions afford better mass separation (compared to protons). To reduce the problem of pulse pile-up and dead-time, low beam currents ($\sim 2-6$ nA) are employed in the analysis. The main contributor to the resolution of the system is the detection system. Most semiconductor detectors employed have resolutions of ~ 25 keV which is ~ 5 channels for an energy calibration of ~ 5 keV/channel.

CHAPTER 3

EXPERIMENTAL

Figure 6 is a schematic of the ion implantation and RBS facility at McMaster used in performing the implantation aspect of the experiments. The electrocatalytic activity measurements were carried out using the electrochemical cell described in Part A of this report.

Figure 7 shows the schematics of the target chamber. The sample is mounted on the goniometer using vacuum grease; and surrounding the sample is an insulated copper tube (cryo-shield) which is thermally connected, but insulated electrically from the cryorefrigerator. The cryo-shield acts as a cryo-pump improving the pressure around the sample to better than 10^{-9} torr which helps to reduce surface contamination, especially carbon, that may result from hydro-carbon evaporation in the diffusion pumps. A copper radiation shield surrounds the cryo-shield and it is continuously cooled by a flow of liquid nitrogen. Secondary electrons are suppressed by applying a -220 V around, but insulated from the target.

The polycrystalline nickel samples annealed in Ar atmosphere were cut into discs ~ 9 mm in diameter, then polished with various grades of emery paper followed by polishing on the rotating wheel using $6 \mu\text{m}$ and finally $1 \mu\text{m}$ diamond paste.

Uniform distribution of implants over a reasonable depth is of interest for electrochemical measurements. To achieve this for

the case of Li (and He) implants a number of Gaussian profiles were summed and the energies and doses so chosen to achieve a predetermined concentration over the depth of interest in Ni. Ion energies of 15 keV, 40 keV and 60 keV in the dose ratio 1:2.1:2.8 respectively were used to achieve a profile that is approximately uniformly distributed between 300-1000 Å. The same technique is employed to achieve uniformly distributed He+ implants in Ni. Here the objective is to obtain the equivalent damage energy distribution as in the Li implants to distinguish between the effect of the dopants and that due to ion implantation produced defects.

1×10^{15} and 1.1×10^{16} ions/cm² of 60 keV Li+ have been directly implanted into polycrystalline nickel, while 1.2×10^{16} and 1.5×10^{16} ions/cm² of 60 keV Li+ have been implanted into NiO discs.

Direct implantation of Ag+ ions into Ni and NiO discs were kindly performed at Chalk River by Dr. J.A. Davies. 1×10^{16} and 4×10^{16} $\frac{\text{ions}}{\text{cm}^2}$ 30 keV Ag+ were implanted into Ni discs while 1×10^{16} ions/cm² 30 keV Ag+ were implanted into NiO.

Recoil implantation of Ag+ ions into Ni and NiO samples have been attempted. The nickel sample had ~ 100 Å silver evaporated on its surface and was then bombarded with $\sim 1.3 \times 10^{16}$ ions/cm² of 60 keV Ar+. A nickel oxide sample with ~ 350 Å of evaporated Ag layer was irradiated with $\sim 1.5 \times 10^{16}$ ions/cm² 120 keV Ar+.

Oxide samples were prepared by thermal oxidation in air at 450° for ~ 20 minutes resulting in ~ 400 Å of NiO layer on the surface.³⁰ One Ni sample was implanted with $\sim 5 \times 10^{17}$ ions/cm² of 25 keV Kr+ in

order to study the effect of the increased surface area that may result from cone formation at this fluence.

All implants were carried out at room temperature. Typical beam currents were $20 \sim 400 \text{ nA/cm}^2$. The beam was first reduced to 2 mm by an off-axis aperture and then x-y swept across a 7 mm aperture in front of the sample. The off-axis aperture ensures that neutral component of the beam did not reach the target. RBS analysing beam current was $\sim 2-4 \text{ nA}$. Doses of $4 \mu\text{C}$ were used to obtain a spectrum.

Each implanted sample was used as anode (oxygen electrode) for oxygen evolution reaction in 30 w/o KOH solution in doubly-distilled water. Before putting the electrode in the solution, electrical connections were spark welded at 7 watts and 10 lb pressure. The back of the electrode and the parts of the lead resting in solution were covered with epoxy coating made from 8 parts epoxy to 1 part hardner. Any traces of epoxy on the implanted surface were removed with acetone and then rinsed in distilled water.

CHAPTER 4
RESULTS AND DISCUSSION

4.1 Uniformly Distributed Implants

Since electrocatalytic activity is essentially a surface effect, and since the whole objective of the implantation is to improve electrocatalytic behaviour, it is desirable to have implanted species whose distribution is fairly uniform over some depth and whose surface concentration is substantial. To achieve this we have used the method of Allen³¹ to sum the different profiles 15-, 40- and 60-keV Li ions in Ni. The individual profiles themselves were derived from the four principal moments using Winterbon Tables. We found that for Li ion energies of 15-, 40-, and 60-keV in the dose ratio 1.2:1:2.8 respectively gives a profile which is approximately uniformly distributed between $\sim 300-1000 \text{ \AA}$ (Fig. 8). A similar procedure was followed to achieve a uniform He⁺ implant distribution in Ni but the overall He⁺ dose was 3 x Li dose. The objective of the He implant is to obtain a similar damage distribution as in the Li implants. The He⁺ ion energies were 15- and 40- keV in the dose ratio 1:1.8 respectively. Figure 9 shows that this distribution is fairly uniform from $\sim 500-900 \text{ \AA}$. Figures 10 and 11 are the results of the SEM examination of Li- and He- implanted surfaces respectively, showing that no significant different surface topography changes result from the two implantations.

The current-potential measurement when these electrodes were used as oxygen electrode in 30 w/o KOH are shown in Figure 12 when the anode current was swept from 100 mA/cm^2 to 0.1 mA/cm^2 and back. Each point on the curve is an average of several sweeps (~ 8), while figure 13 gives similar measurements but with the current sweep now between 1000 and 0.1 mA/cm^2 . The current-potential curves obtained for the first and second days of measurements are indicated in the figure. Also shown in the figure for comparison is the $i-v$ relationship obtained for an un-implanted sample. Two things are obvious from these curves:

1. The curves obtained for the implanted electrodes are similar in form to that for the unimplanted electrode, and in absolute terms there is little or no reduction in cell potential due to these implants.
2. The departure of the current-potential measurements obtained during the first day from that obtained the second day is less for the implanted samples than for the pure Ni electrode, suggesting an improved electrode stability due either to the dopants or to the implantation process. Figure 14 compares the microscopic nature of the Ni electrode surface (a) Li-implanted NiO, (b) between He implanted electrode and unimplanted electrode and (c) between unimplanted and Li implanted electrode. We note that the corrosion product on the surface of the implanted electrodes are more uniform than that of the unimplanted Ni electrode.

4.2 Li-implanted Ni Electrodes

Figure 15(a), (b) show the current potential relationships obtained for a nickel electrode implanted with 1.1×10^{16} Li ions/cm² at 60 keV. The low current density curve is plotted on linear scale, while the high current density part is in semilog scale. As in Figs. 12 and 13, two Tafel regions of each curve - the regions with different slopes - are noticeable. Compared to figures 12, 13 there is also no noticeable reduction in the cell potential but a higher degree of reproducibility especially at the higher current densities is evident in Fig. 15(b). The departure from reproducibility ~ 25 mV. Figure 16 (a),(b) show the microscopic nature of the electrode surface. The dendrite-like features at high magnification are thought to be KOH as confirmed by litmus and flame tests.

4.3 Li Implanted NiO Electrode

Figure 17(a) and (b) show the i-v curves obtained for oxygen evolution on the Li implanted NiO electrode. The Li dose was 1.5×10^{16} ions/cm². The cell potential at all current densities is higher than that obtained for either the electrode implanted with less Li+ dose than 1.5×10^{16} ions/cm² or the unimplanted electrodes. It is only the second day measurements which approaches that of the Ni electrodes implanted with 1.1×10^{16} Li ions/cm². The degree of reproducibility is also the worst among those considered in sections 4.1 to 4.3. Optical micrograph of this electrode's surface shows no trace of corrosion products whatsoever (Fig. 14d).

The atomic density of Ni is $\sim 9 \times 10^{22}$ atoms/cm³. Therefore the implantation of 1×10^{15} Li⁺ ions/cm² corresponds to ~ 0.1 atomic % and 1.1×10^{16} Li ions/cm² is equivalent to ~ 1.2 at % while 1.5×10^{16} Li ions/cm² corresponds to ~ 1.6 at %.

Tseung et al.⁴ have reported dramatic increases in the conductivity of NiO with increase in Li doping. They prepared their electrodes by mixing the powders with aqueous dispersion of Ptfе (I.C.I.G.P.I. Fluon Dispersion) and brushing the result on to a nickel screen. Surface-area measurements carried out by them show a maximum area for those samples containing between 0.1 and 0.5 atom-% Li and attributed this higher surface area to the preferential filling of the cation vacancies by lithium ions. They observed an abnormally high electrocatalytic performance in the electrode with the abnormally high surface area (0.1 at % Li) and concluded that the dominant effect is a surface effect rather than a conductivity effect.

We consider the result above to be in general agreement with that of Tseung above. If the catalytic effect is mainly due to the dopant concentration as they concluded then we should have been able to see a favourable reduction in the cell potential for the electrodes implanted with 1.1×10^{16} (1.2 at %) and 1.5×10^{16} (1.6 at %) Li. Conversely the fact that there was no reduction in cell potential suggests that at these doses, Li (or He) implantation does not cause any appreciable increase in the surface area of nickel or nickel oxide. Also using the empirical rules for substitutionality in implanted metastable surface alloys proposed by Sood²⁶ it is evident that Li cannot form substitutional metastable alloys with Ni.

4.4 Ag-implanted Ni Electrode

(i) 1.0×10^{16} Ag⁺ ions/cm² in Ni

The current-potential measurements obtained for this electrode are shown in Figure 18(a) (for low current densities) and Figure 18(b), for higher current densities. Comparison of Figures 18(a), (b) with that of pure Ni (Figs. 11 and 12) shows a favourable reduction of cell potential by $\sim 6\%$ (at low current densities 100 mA/cm²) and up to $\sim 40\%$ (at the highest current density used). The potentials at the lowest current densities (0.1 to 10.0 mA/cm²) remain approximately the same emphasizing the fact that a threshold potential is required to break down water into its ions.

(ii) 4×10^{16} Ag⁺ ions/cm² in Ni

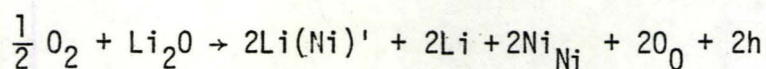
Figures 19(a) and 19(b) show the current-potential curves for the Ni electrode implanted with a high dose of 4.0×10^{16} Ag⁺ ions/cm² which again shows a marked reduction in the cell potential over an unimplanted (and also Li-implanted) electrode.

Both implants in 4.3(i) and (ii) were carried out at 50 keV. There is a remarkable agreement between the curves obtained during the first day of measurements with that obtained the following day; and also among the electrodes implanted with 1×10^{16} Ag⁺ ions/cm² and that implanted to 4×10^{16} ions/cm². Thus a dose-dependent effect is not easily discernible, and more experiments will have to be done to determine the influence of Ag dose and energy on

electrocatalytic behaviour of the silver-implanted oxygen electrode.

Figure 20(a) and (b) shows the optical micrographs of the Ag implanted Ni electrode after electrochemical measurements and the absence of corrosion products on the surface testifies to the ability of Ag as a corrosion resistant material.

The mechanism by which Ag influences electrocatalytic behaviour is not yet understood and there is very little information in the literature in this regard. The atomic radius of Ag is 1.44 Å and its electronegativity is 1.9. Therefore according to the empirical rule of Sood, Ag can form substitutional metastable alloys with Ni (atomic radius 1.24, electronegativity 1.8). If Ag forms substitutional alloys with Ni then the incorporating reaction is probably similar to that of Li_2O in NiO:



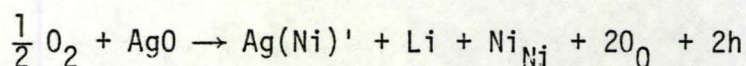
where

$\text{Li}(\text{Ni})'$ is lithium atom in Ni site and has negative charge

Ni_{Ni} is nickel in nickel site

O_0 is oxygen in oxygen sites

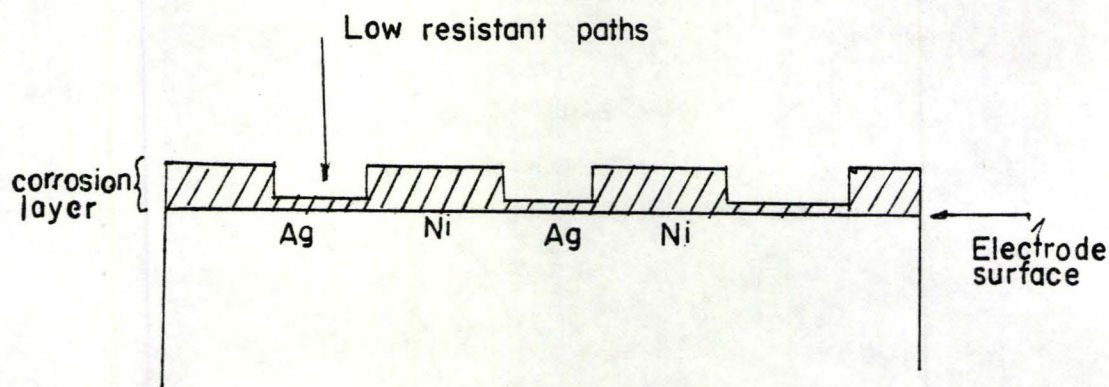
For Ag being substitutional in NiO lattice we have



The range of 50 keV Ag ions in nickel will be considerably less than the range of 60 keV Li ions in Ni; therefore in comparison with Li in nickel most of the implanted Ag will be near the nickel surface. Also the bigger size of the Ag atoms will tend to squeeze the Ni atoms

thus effectively creating conduction paths.

Another possibility is to look at the Ag atoms as segregating together inwardly into the Ni or outwardly - either way they form paths highly resistant to corrosion surrounded by easily corroded nickel sections:



RBS analysis of the Ag-implanted electrodes before and after electrochemical measurements indicates that no Ag was lost during the measurements as seen in the RBS Spectra before and after electrochemical measurements - Fig. 20(c).

4.5 Recoil Implanted Ag in Ni, NiO

Figure 21(a), (b) are the current-potential measurements for the Ag recoil-implanted nickel electrode. No improvement in cell potential are observed either at low or high current densities. The same trend is observable in Fig. 22(a),(b) which are the curves obtained for Ag recoil implants into Ni at Ar energy of 120 keV and 1.5×10^{16} ions/cm² Ar fluence. The reason is probably due to the fact that

all the remaining Ag are part of the evaporated layer and not recoil implanted species. An indication of this also shows in the RBS spectra where the Ni substrate surface has not completely moved forward to where it should be exposed at the surface, Fig. 22 (a),(b).

4.6 Kr⁺ Ion Implanted Ni Electrode

This electrode has the highest cell potentials of all the electrodes tested. The electrode was implanted with a high Kr⁺ ion dose ($\sim 5 \times 10^{17}$ ions/cm²) the regime where cones are expected to form.³² The cones probably formed and the poor catalytic behaviour (much worse than for polished nickel) may be due to the high concentration of Kr near the surface. One way to get around this will be to anneal the electrode after Kr bombardment at such temperature (where the cones are still thermally stable) in order to desorb the inert gas and therefore take advantage of the increased electrode surface area due to cone formation.

4.7 Overpotential and Kinetic Parameters of the Test Electrodes

4.7.1. Electrode Potential

Table 1 gives the various electrode potentials measured at current densities of 100 mA-, 200 mA- and 1000 mA/cm² on the different test electrodes examined in this experiment. The time-variation of these potentials are indicated by showing the values of the electrode potential for the 1st and 2nd days of measurements. All potentials were measured vs DHE (whose overpotential throughout the experiment was $\sim 40-45$ mV). No corrections were made for either the IR drop or the overpotential of

DHE. An electrode potential of 1.80 volts at 200 mA/cm^2 obtained on polished Ni compares with 2.17 V reported by Miles et al.² at 80°C in 50 w/o KOH. Also the measured potential of 1.715 V at 100 mA/cm^2 on polished Ni is in good agreement with most reported data at this current density in 30 w/o KOH at 80°C . The measured electrode potentials on polished Ni electrode within the accuracy of these measurements is the same as that observed with the electrode pre-oxidised in air ($\sim 400 \text{ \AA}$ oxide). As mentioned previously this may be due to the fact that the polished electrode was rapidly covered with a thin layer of oxide once oxygen evolution begins.

Both the He-implanted electrode and $\sim 1 \times 10^{15} \text{ Li}^+$ ions/ cm^2 implanted Ni electrodes show a marginal reduction of $\sim 50 \text{ mV}$ in electrode overpotential at 100 and 200 mA/cm^2 whereas no reductions were observed at the higher current densities ($\sim 1000 \text{ mA/cm}^2$). Also, Ni and NiO electrodes implanted with higher concentration of Li^+ ($\sim 1.6 \text{ at } \% \text{ Li}$) show no potential reduction. These effects may be due to

- (a) The distribution of the lower concentration Li (and He) implants were chosen to be fairly uniform by a choice of energies and dose ratio. In effect, most of the Li will be near the surface. In contrast the higher concentration implants were carried out at 60 keV with a peak concentration that is farther from the surface than the uniformly distributed case.
- (b) We have no evidence that the implanted Li remains in the electrode, or it may even have been redistributed.

The Ag implanted electrode results in a considerable reduction in electrode potential especially at the higher current densities (1.68 V at 200 mA/cm² compared to 1.8 V for polished Ni; and 2.17 V at 1000 mA/cm² compared to 2.75 V for polished Ni) where a reduction by ~600 mV was observed. However, at the moment we can say very little about the dependence of this reduction with Ag dose since the electrode potential is quite similar for both 1×10^{16} Ag ions/cm and 4×10^{16} Ag ions/cm² implants into Ni.

4.6.2 Kinetic Parameters

Figures 26(a) to 26(e) show the curves of overpotential versus log of current density for some of the test electrodes. A reversible cell potential of 1.2 volts has been used. From these curves the kinetic parameters - exchange current density, i_0 , Tafel slope, b , and transfer coefficients - have been determined. Each curve exhibits a dual Tafel region, one at low and the other at high overpotentials. The kinetic parameters for oxygen evolution between 0.1 - 150 mA/cm² are shown in Table 2 while Table 3 shows the equivalent parameters for polarisations up to ~1,500 mA/cm².

The Tafel slopes for all test electrodes are similar at low overpotentials underlining the fact that there is a minimum potential necessary to break down water into its ions. The observed Tafel slope of ~0.06 - 0.07 volts/decade of current compares with $b = 0.095$ reported by Miles et al.² at the same temperature but in 50 w/o KOH.

From the obtained Tafel slopes, the transfer coefficients have been calculated and the calculated value of ~1.1 at low overpotentials

is considered consistent with an electron transfer step being rate-determining in the oxygen evolution process. The higher slopes for all the test electrodes in the higher current density region might be due to other processes occurring simultaneously with oxygen evolution on the electrodes. It is plausible that some nickel oxide formation took place at the higher current densities. A similar observation for hydrogen evolution on Pb in 6N KOH solution at 25°C has been reported by Lee,¹ and by Miles et al.² for oxygen evolution reaction on Ni at 208°C in 50 w/o KOH. The absence of any hysteresis effect (within experimental errors) probably indicates the instability of the formed oxide with polarisation.

By extrapolating the linear regions of the Tafel plot to the log of current density axis we obtain the exchange current density i_0 . The values of i_0 obtained at the low current density and high current density regions are also shown in Tables 2 and 3. A value of $i_0 \sim 10^{-8}$ A/cm² at 80°C obtained in this report at low current density compares with $\sim 10^{-10}$ A/cm² reported in Bockris² at 25°C and 0.1 N NaOH. At the intermediate current density, we obtained $i_0 \sim 10^{-3}$ A/cm² and $i_0 \sim 10^{-1}$ A/cm² for high current density region (~ 1500 mA/cm²).

4.8 RBS Analysis from Ag Implanted Electrode

Figure 20(c) shows the Rutherford Backscattering spectra from Ni and NiO electrodes implanted with 1×10^{16} Ag⁺ ions/cm² at 50 keV. Also included is the spectrum from Ni implanted with 3×10^{16} Ag⁺ ions/cm². The spectrum from the Ni implanted with 1×10^{16} Ag⁺ ions/cm² was taken after the sample has been used as oxygen electrode while the other two spectra were taken before electrochemical measurements.

Analysis of the spectra shows that the Ag-implanted Ni electrode contains $\sim 1.08 \times 10^{16}$ Ag atoms/cm² after electrochemical measurement which is approximately the same amount of Ag in the NiO sample that has not been used as oxygen electrode. Thus the spectra indicate that no Ag was lost as a result of using the Ag-implanted Ni as oxygen electrode in 30 w/o KOH solution at 80°C.

Figure 20(d) shows the depth distribution of implanted Ag atoms in nickel determined for the sample that has been employed as oxygen electrode, and for the as-implanted Ni sample. Within the detector resolution it appears that the silver atoms are distributed deeper in the substrate after electrochemical measurements. If Ag diffusion occurs the peak concentration would not be expected to move appreciably. However we do know that nickel oxide forms on the Ni surface. Thus if an oxide layer is formed (as expected) during the polarization measurements then nickel atoms would have diffused forward to form a thicker oxide layer. However we did not see any indication of any oxygen on the surface using RBS technique. It may well be that the oxide layer is too thin for the resolution of this technique. The movement of the Ag peak position $< 100 \text{ \AA}$ which is small in regard to the detector resolution. NiO probably acts as a barrier preventing Ag migration to the electrode surface and thus prevents Ag loss. As the oxide layer grows, the Ag will be buried deeper.

Figure 24 shows the RBS from Ag recoil implanted Ni while Fig.25 shows a similar spectra from NiO. Each sample had a thin layer of Ag evaporated on its surface and was subsequently bombarded with Ar⁺ ions. The change in slope of the Ni-edge in both figures indicate

that atomic mixing between Ni and Ag, and between NiO and Ag has begun. As Ar⁺ ion bombardment proceeded in addition to atomic mixing near the interface, erosion of the silver layer due to sputtering would occur at the same time. As a result the analysing He beam is able to scatter from the Ni atoms with higher energies and hence the Ni surface progressively moves forward. When there is no more evaporated Ag layer on the surface, and when mixing over a thin layer has occurred the nickel surface would have moved sufficiently forward to where it should be when the He ions with incident energy E_0 (1 MeV) scattered off nickel atoms at the surface. The fact that the Ni surface in Figs. 24 and 25 has not moved forward sufficiently indicates the surface is still pure Ag. It is interesting to note that electrodes having only small amounts of Ag incorporated in them gave better performance than those having pure Ag on the surface.

CHAPTER 5

CONCLUSIONS

1. At doses of $\sim 1 \times 10^{15}$, 1.1×10^{16} ions/cm² and 1.3×10^{16} ions/cm² 60 keV Li⁺ or 3×10^{15} ions/cm² He⁺ ions in Ni does not seem to produce any appreciable effect in the electrocatalytic activity of nickel when used as the oxygen electrode in 30% KOH solution at 80°C but do cause a reduction in the rate of corrosion product formation.
2. $\sim 1.5 \times 10^{16}$ ions/cm², 30 keV Li⁺ ions in $\sim 400 \text{ \AA}$ NiO thermally grown in air does not cause a reduction in the cell potential when the electrode was used for oxygen evolution in 30 w/o KOH solution at 80°C..
3. Recoil implantation of Ag⁺ atoms with Ar⁺ ions of 120 keV (at 1.5×10^{16} Ar⁺ ions/cm²) into NiO or 60 keV Ar⁺ ion (at 1.2×10^{16} Ar⁺ ions/cm²) into Ni, do not seem to have any beneficial effect either on the cell potential or formation of corrosion product at the oxygen electrode.
4. 1×10^{16} ions/cm² and 4×10^{16} ions/cm² of Ag⁺ ions implanted into nickel improved the electrocatalytic activity of the electrode by as much as 6% (at the lower current densities) and 40% (at the highest current density used (= 1000 mA/cm²)). These effects are suggested to be due to either the formation of substitutional metastable alloy between nickel and silver, or the aggregation of the silver atoms to form a less corrosible low resistance path for charge exchange.

5. Dual Tafel regions were observed for each test electrode. The higher Tafel slope at the higher current densities are thought to be due to formation of some nickel oxide simultaneously with oxygen evolution.
6. The observed Tafel slope of ~ 0.07 at the low current density is thought consistent with an electron transfer step being rate-determining.
7. RBS analysis of the Ag-implanted Ni electrode before and after polarisation measurements indicates that no Ag was lost in the process of electrochemical measurements.

CHAPTER 6

SUGGESTIONS FOR FURTHER WORK

1. The improvement of electrocatalytic activity of nickel with silver dose is unclear at the moment and deserves further investigation.
2. The role of silver and its mechanism in improving the electrocatalytic activity of nickel for oxygen evolution is now at best only speculative.
3. While Soods²⁶ empirical rule suggests that lithium and nickel do not form substitutional metastable alloys, some authors⁸ have reported improved catalytic behaviour with lithium dope in Ni. It will be necessary to resolve whether their observation is mainly due to a high surface area effect or to the concentration of lithium in the electrode.

Table 1: Measured electrode potentials on test electrodes for oxygen evolution in 30 w/o KOH at 80°C.*

Electrode	Electrode Potential vs DHE (volts) at Various Current Densities					
	100 mA		200 mA		1000 mA	
	1st day	2nd day	1st day	2nd day	1st day	2nd day
Polished Ni	1.715	1.675	1.80			
Thermally Grown NiO	1.722	1.655	1.80	1.798	2.75	2.75
He implanted Ni	1.735	1.710	1.85	1.825	2.85	2.80
He implanted Ni	1.652	1.660	1.752		2.752	2.75
Li implanted Ni 0.1 at % Li	1.670	1.655	1.752	1.752	2.78	2.78
1.2 at % Li	1.735	1.710	1.825	1.825	3.05	3.05
Li implanted NiO: 1.6 at % Li	1.840	1.714	1.90	1.825	3.0	2.85
Ag implanted Ni: 1×10^{16} Ag ions/cm ²	1.644	1.625	1.680	1.680	2.175	2.175
4×10^{16} Ag ions/cm ²	1.680	1.657	1.72	1.71	2.38	2.38

*Potentials were measured vs DHE and were not corrected for IR drop.

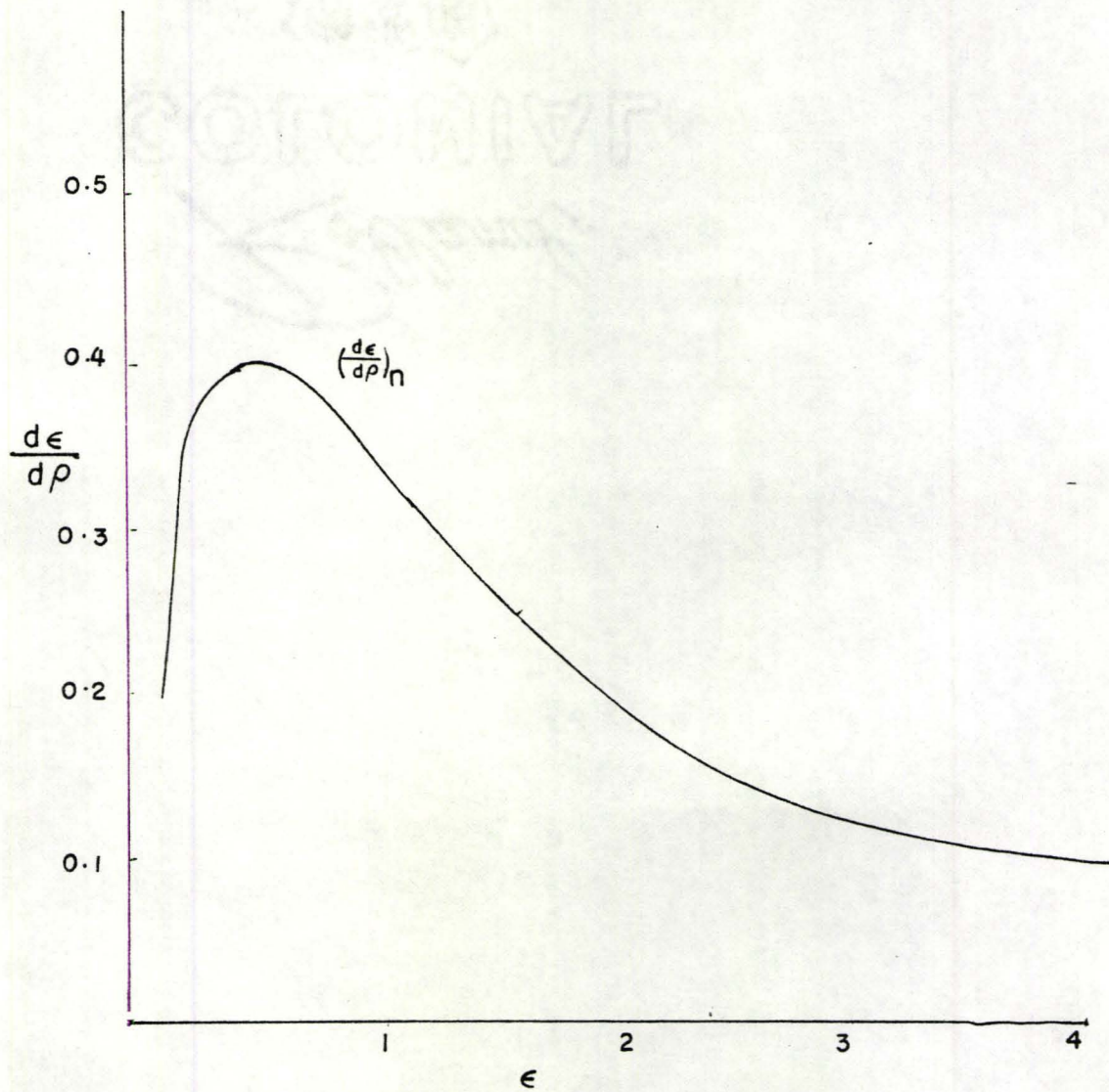
Table 2: Kinetic parameters for oxygen evolution on test electrodes for galvanostatic sweep from 0.1 - 150 mA/cm².

Electrode	Tafel Slope b(V)		Exchange Current Density A/cm ²		Transfer Coefficient α^*	
	Low η	High η	Low η	High η	Low η	High η
Polished Ni	0.064	0.310	3.5×10^{-8}	2×10^{-3}	1.098	0.227
He implanted Ni	0.04	0.290				
1.0×10^{16} Li ⁺ ion/cm ² Implanted Ni	0.05	0.30	1×10^{-8}	2×10^{-3}	1.17	0.39
1×10^{16} Ag ⁺ ions/cm ² Implanted Ni	0.053	0.217	3.5×10^{-8}	8×10^{-4}	1.326	0.324
1.5×10^{16} Li ⁺ ions/cm ² NiO	0.06	0.305	9×10^{-9}	1.6×10^{-3}	1.17	0.230

$$* \alpha = \frac{2.303 RT}{bF}$$

Table 3: Kinetic parameters for oxygen evolution on Ni electrodes implanted with various species. Current sweep from 0.1 - 1,500 Ma/cm².

Electrode	Tafel Slope b volts		Exchange Current Density A/cm ² i_o	Transfer Coefficient α $\frac{2.303 RT}{b}$	
	Low η	High η	High η region	Low η	High η
4×10^{16} Ag ion/cm ² in Ni	0.07	1.98	2.50×10^{-1}	1.0	0.035
1×10^{16} Ag ions/cm ² in Ni	0.07	1.88	2.7×10^{-1}	1.0	0.037
1.1×10^{16} Li ion/cm ² in Ni	0.07		3.0×10^{-1}	1.0	
1.5×10^{16} Li ion/cm ² in NiO	0.07		3.0×10^{-1}	1.0	
Polished Ni	0.064			1.17	



Figures 1 : Rate of ion energy loss.

1. - Nuclear

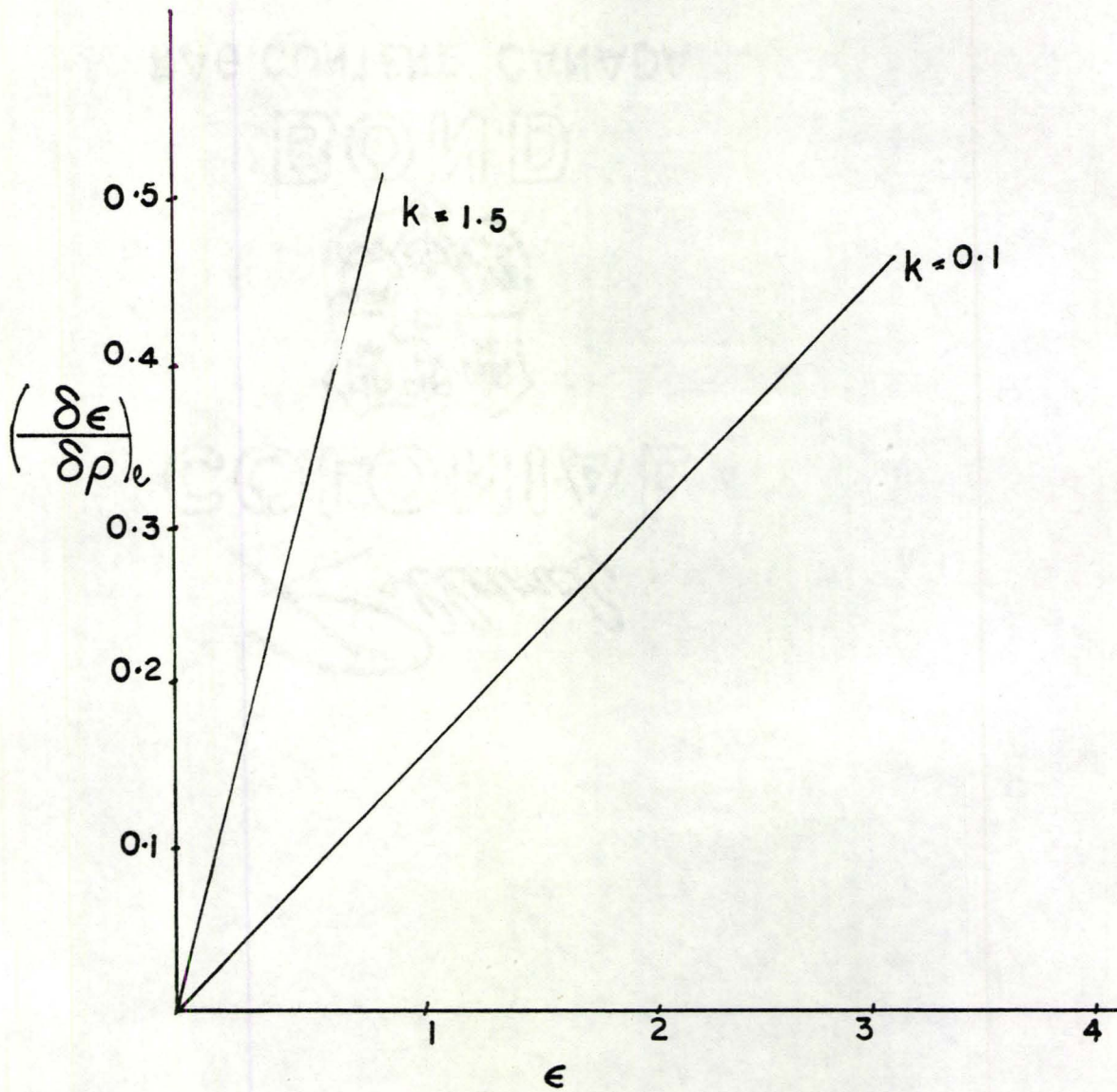


Figure 2: Rate of Energy Loss (electronic).

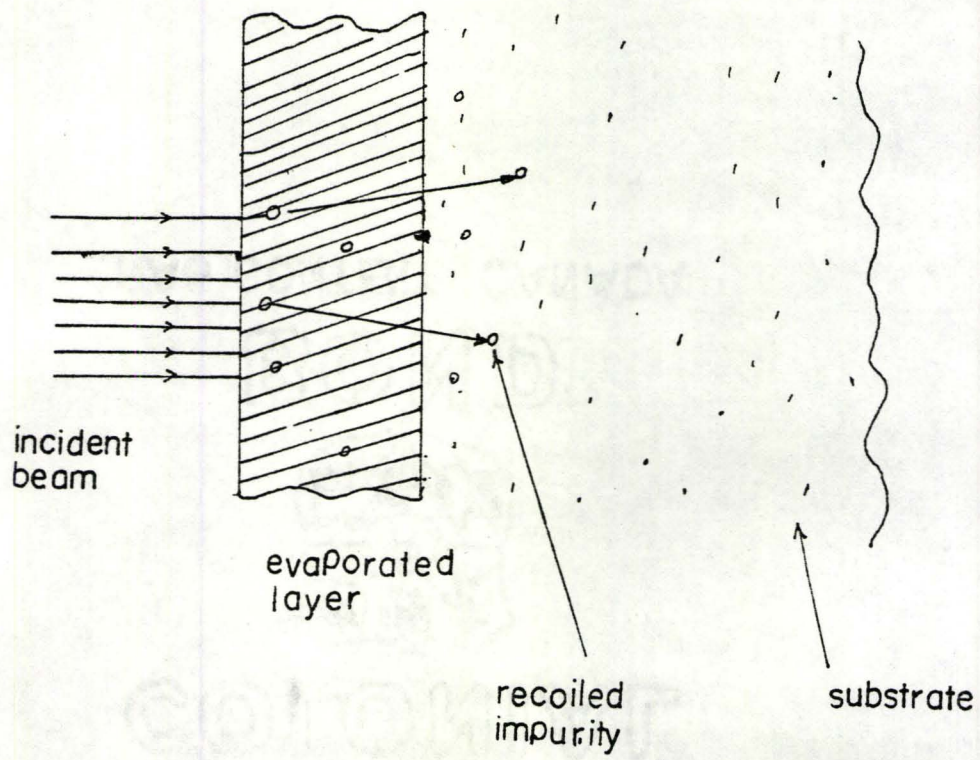


Figure 3: Illustration of recoil implantation.

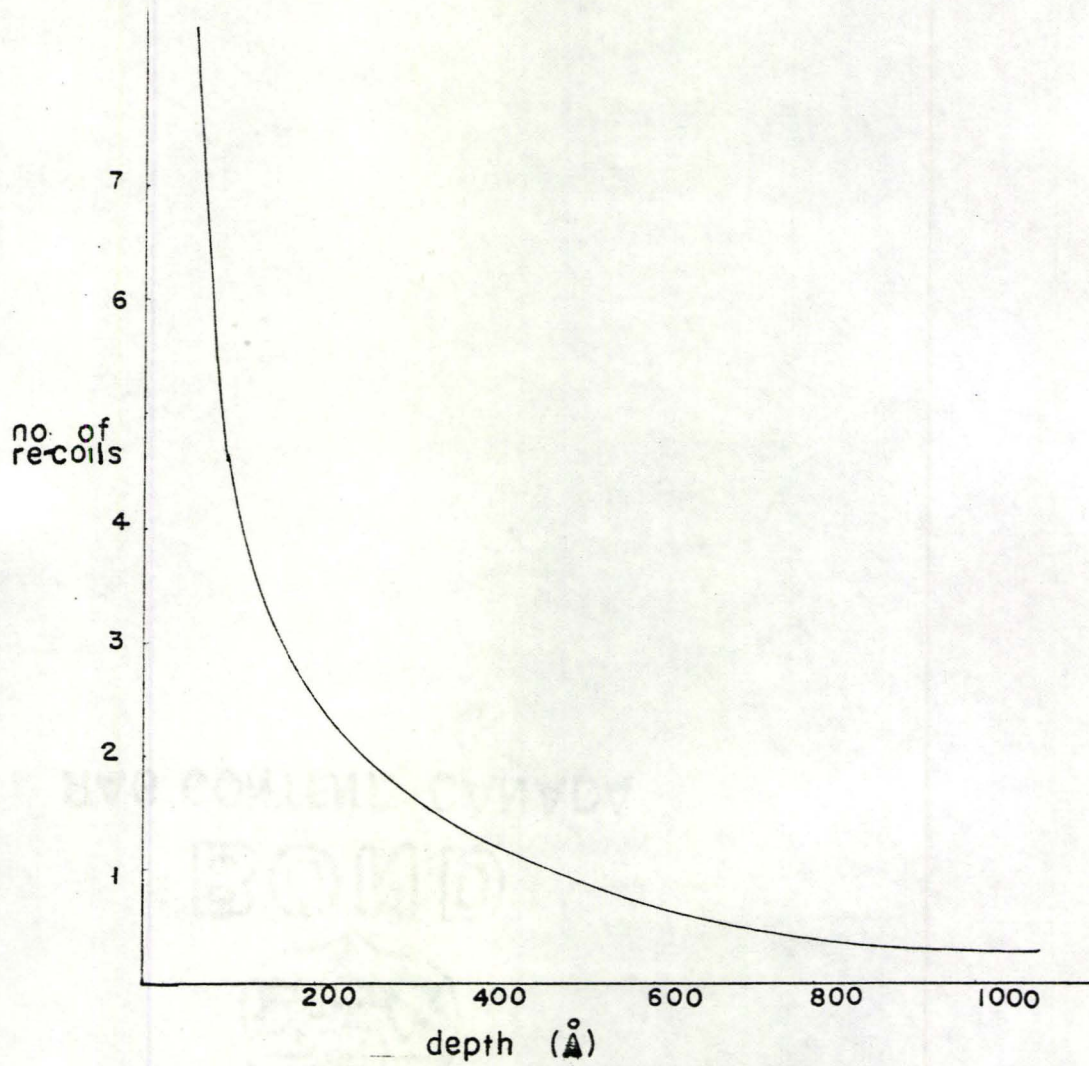


Figure 4: Distribution of recoil-implanted atoms. (After Ref 44).

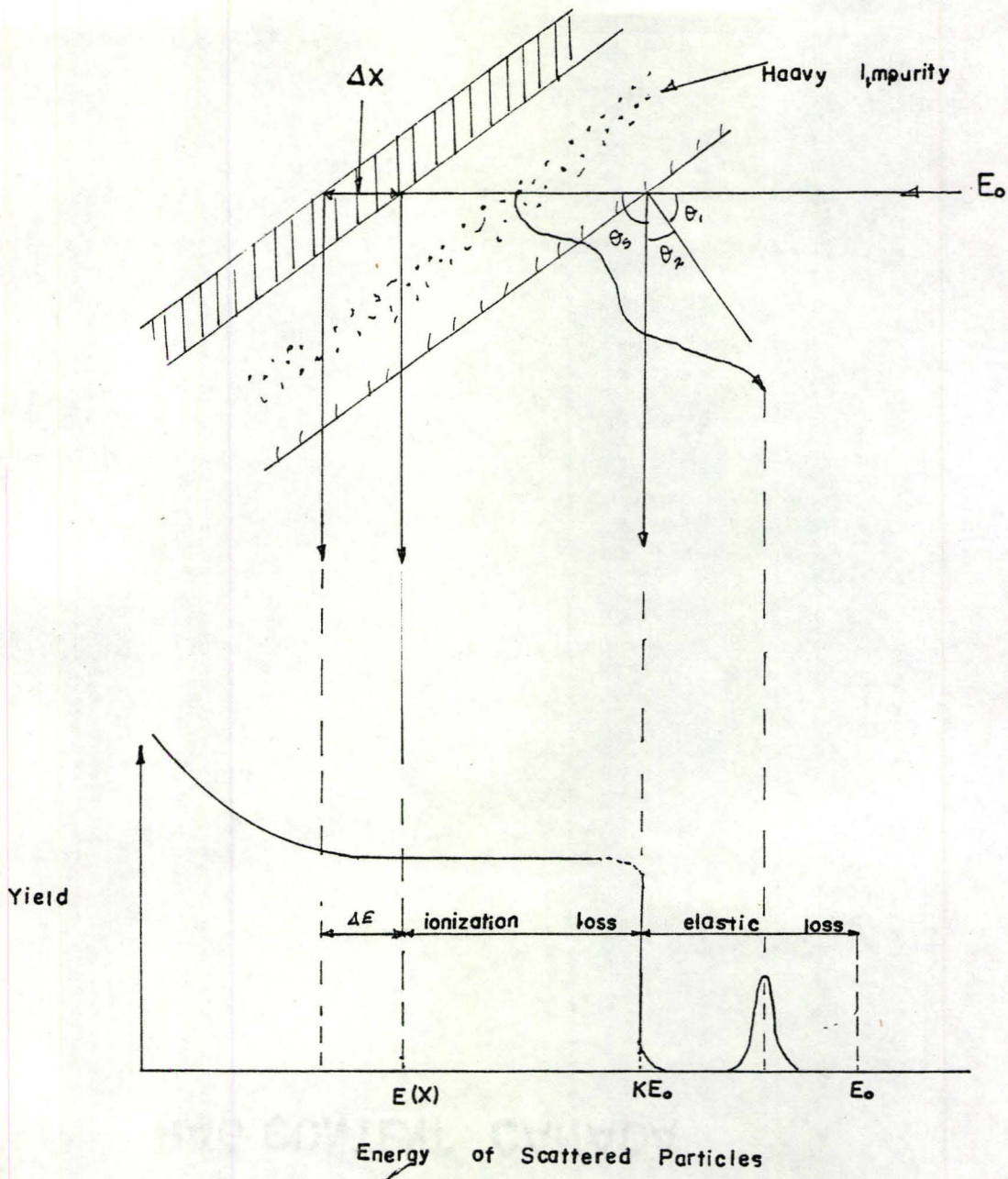


Figure 5: Principle of Elastic Backscattering (after Bogh 1968).

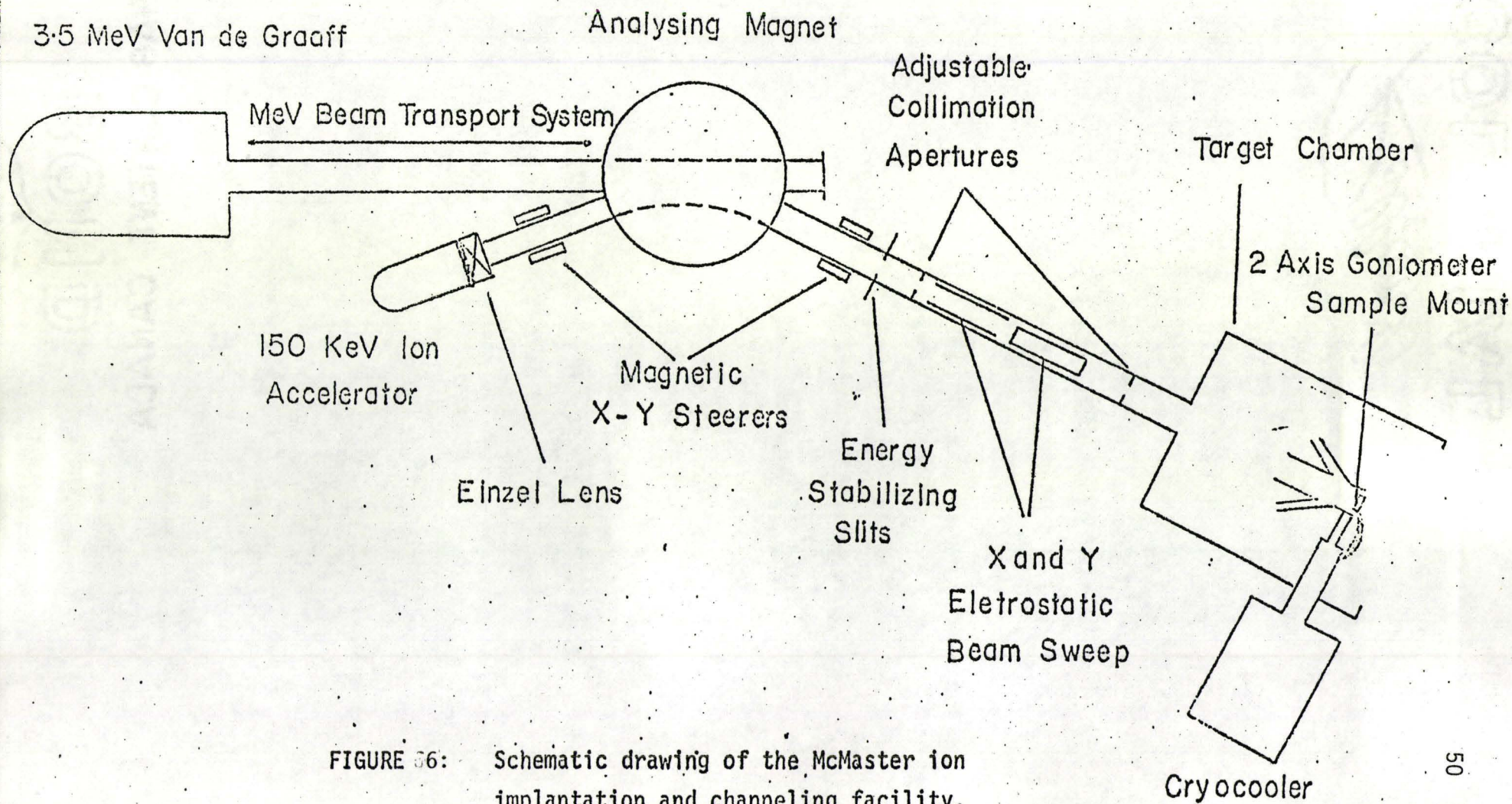


FIGURE 36: Schematic drawing of the McMaster ion implantation and channeling facility.

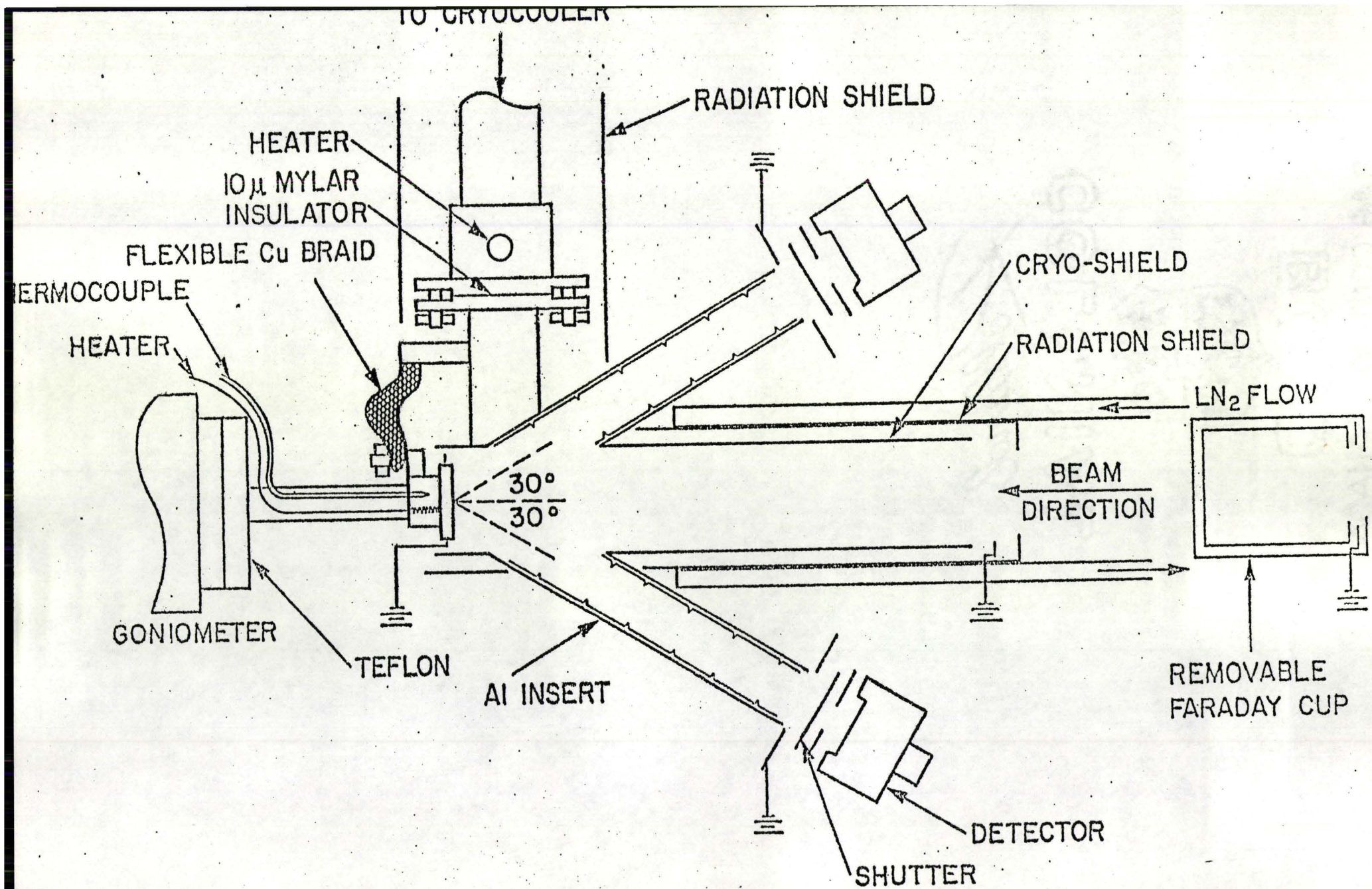


FIGURE 7: Schematic drawing of target chamber.

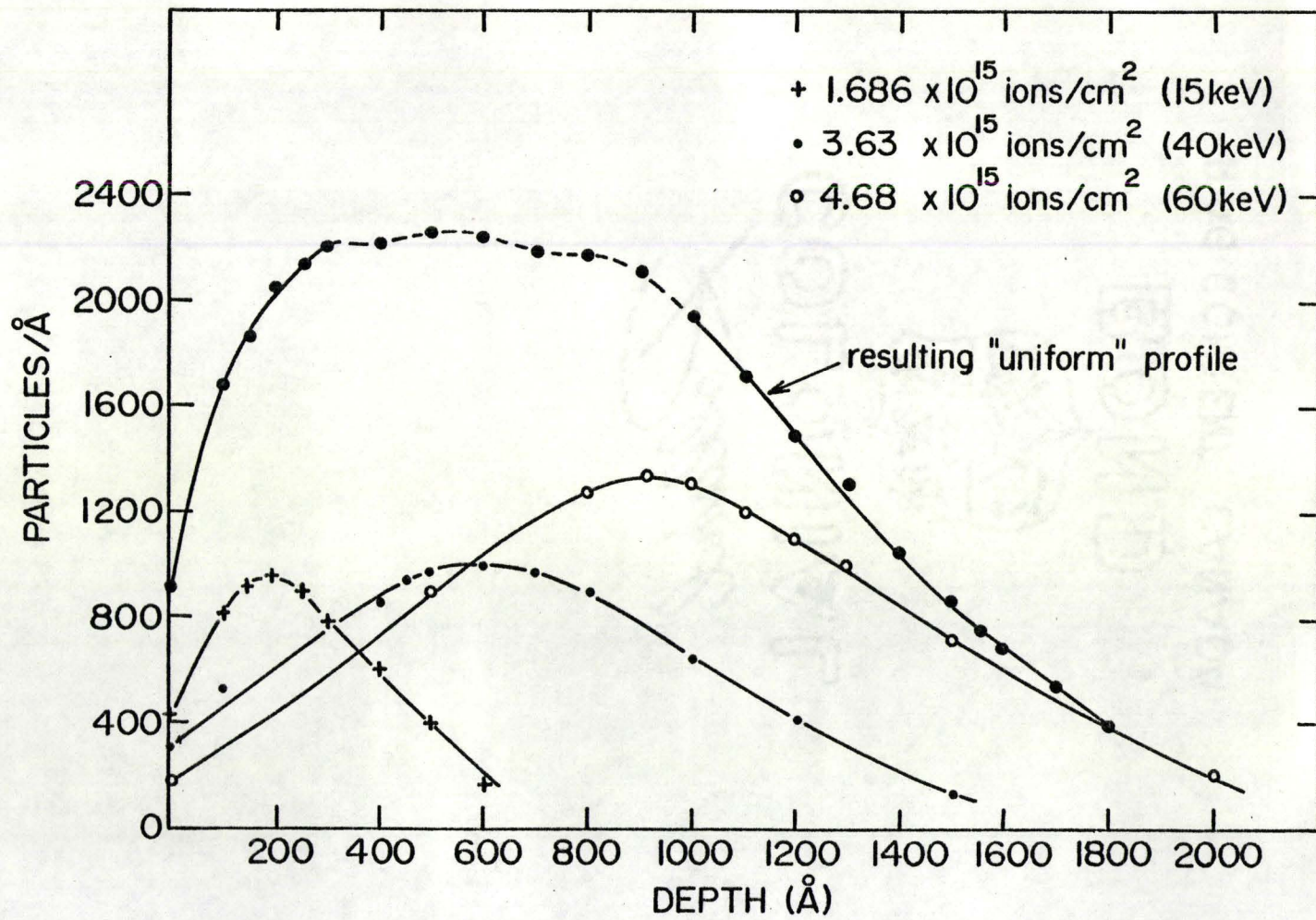


Figure 8: Uniform distribution of implanted Li atoms.

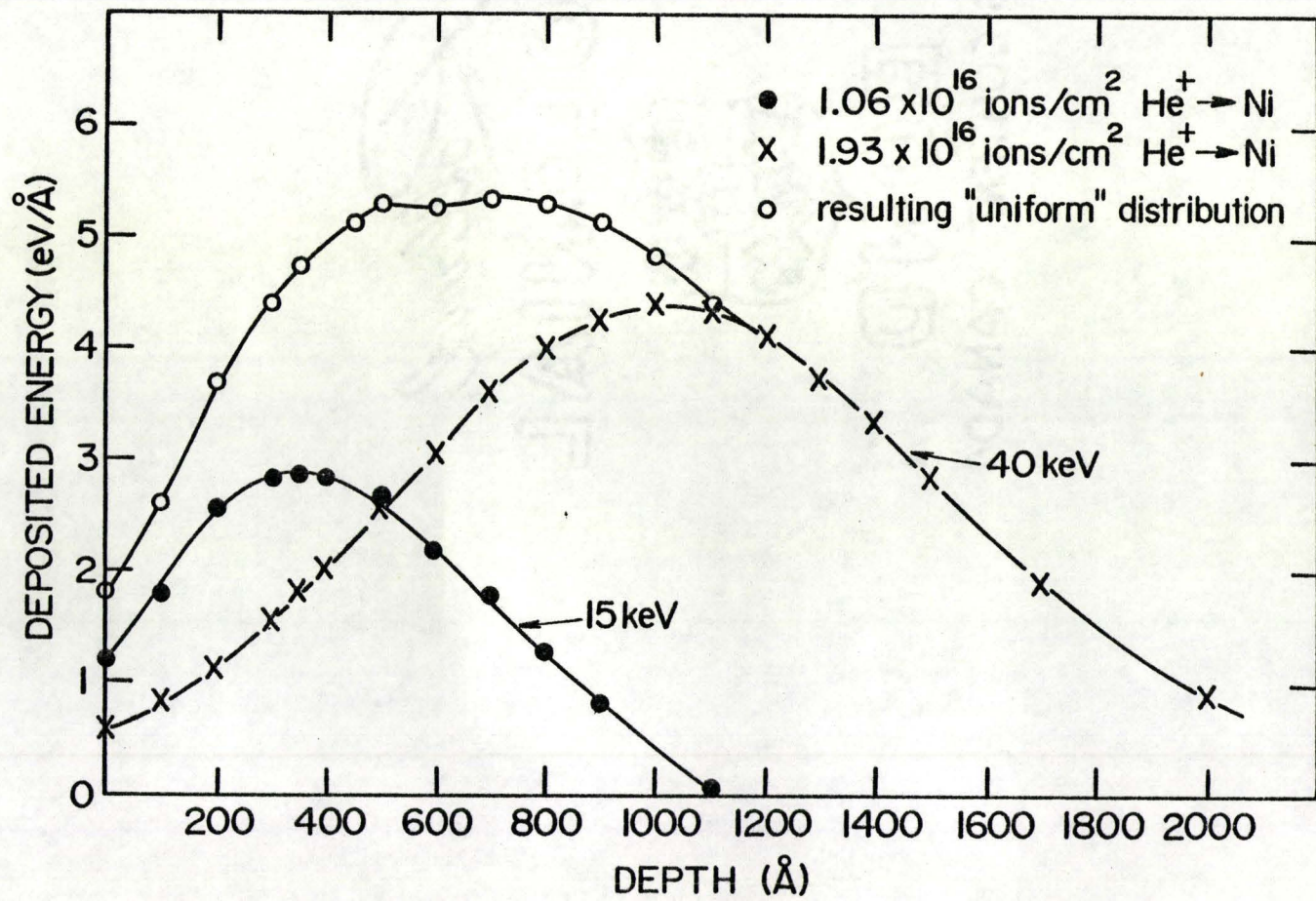


Figure 9: Uniform distribution of implanted He atoms.

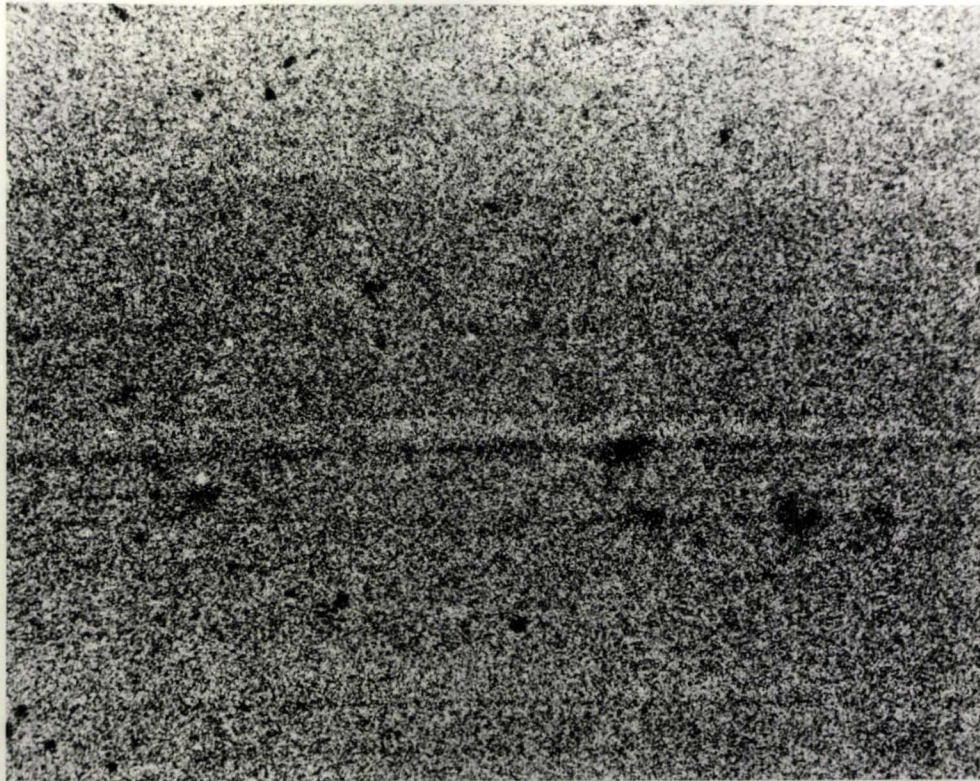


Fig. 10 S.E.M. picture of Li implanted Ni.

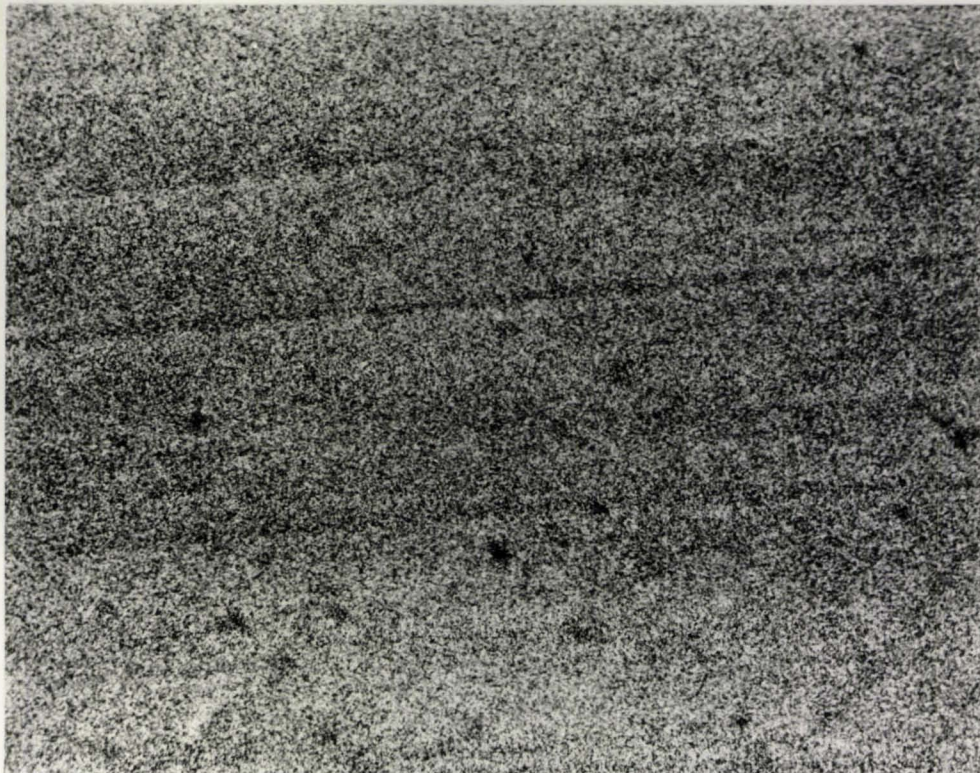


Fig. 11 S.E.M. picture of He implanted Ni.

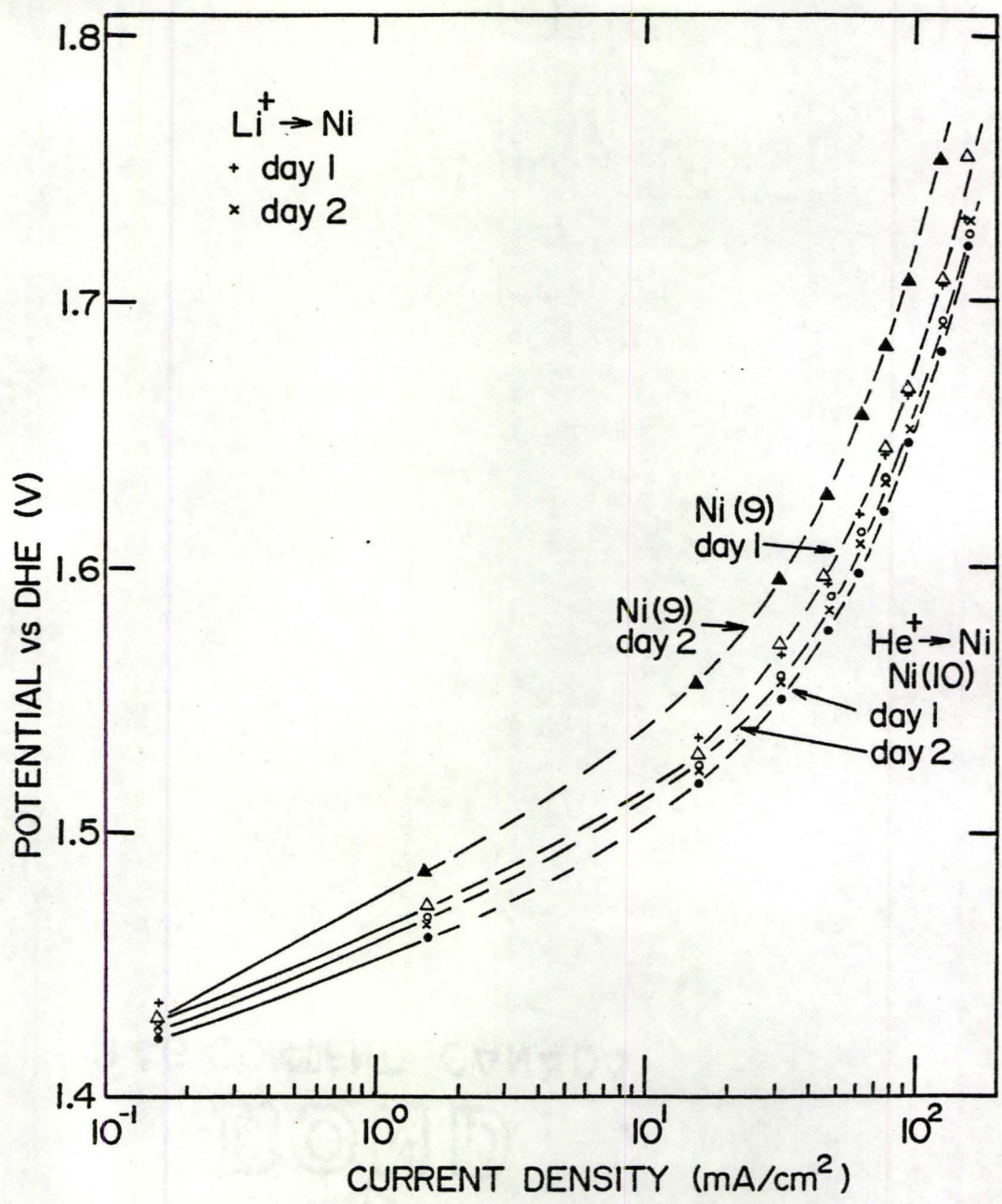


Figure 12: Current potential curve for Li- and He-implanted Ni electrode (low current density).

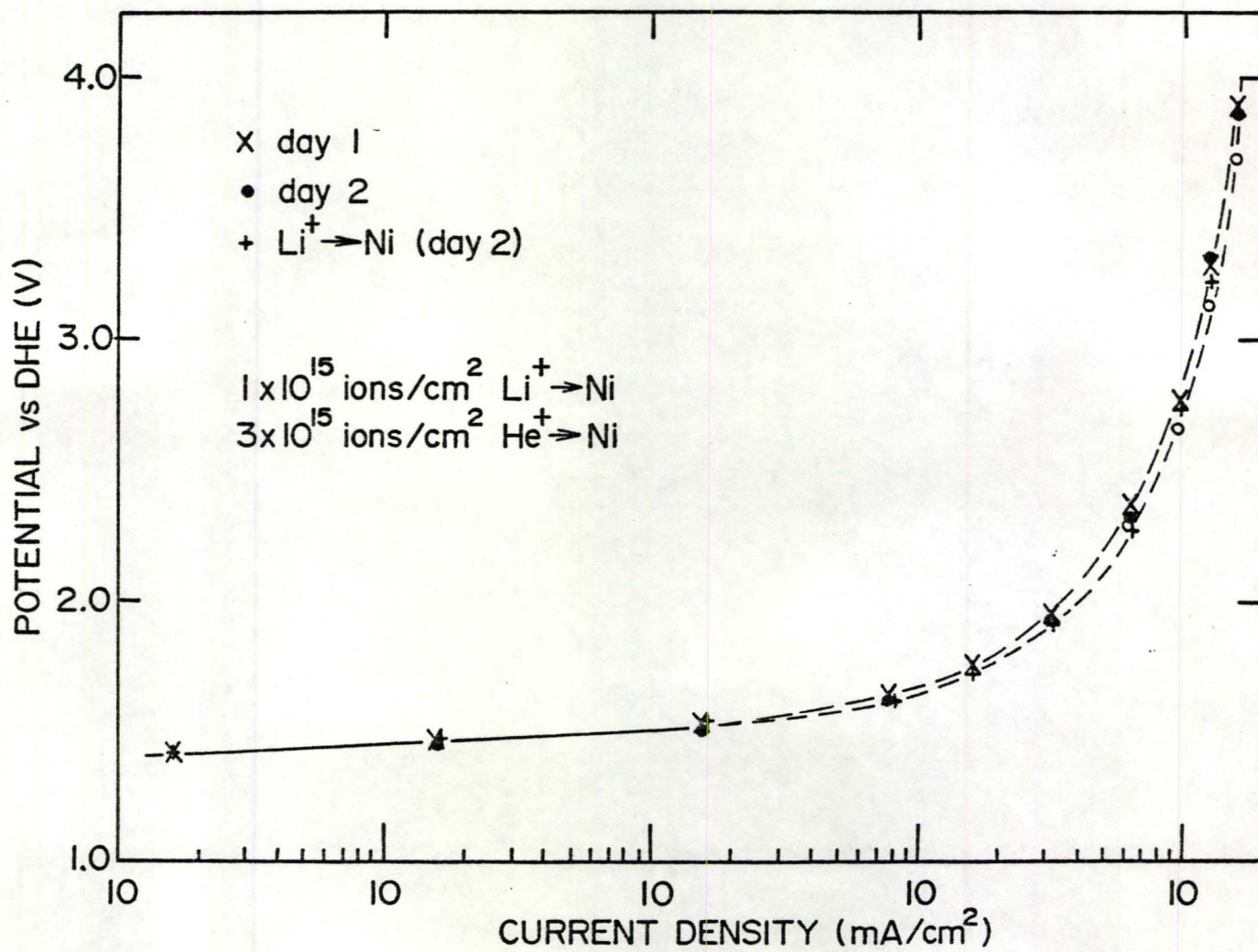
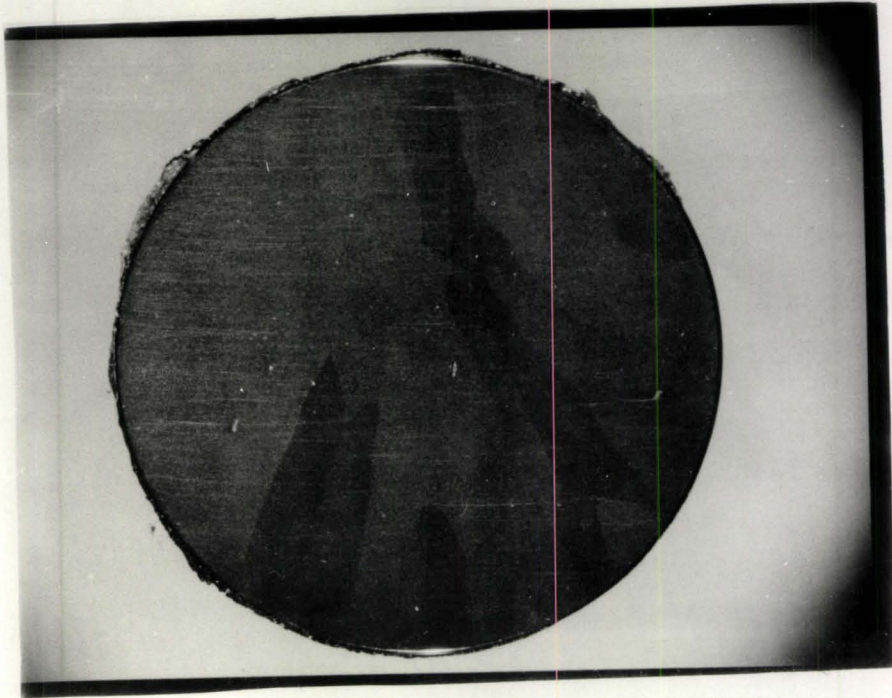
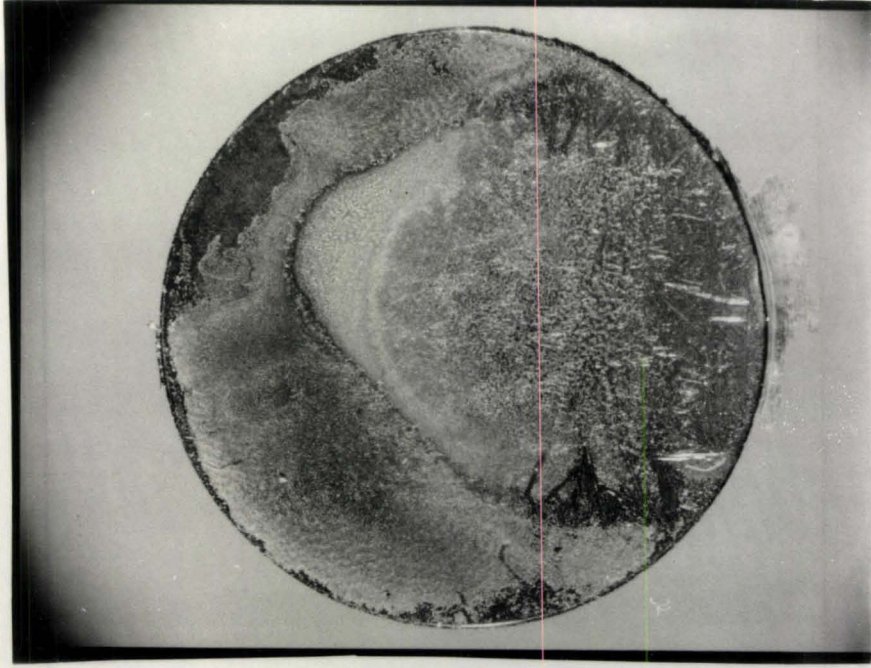


Figure 13: Current-potential curve for He-, Li-implanted Ni electrode (high current density).



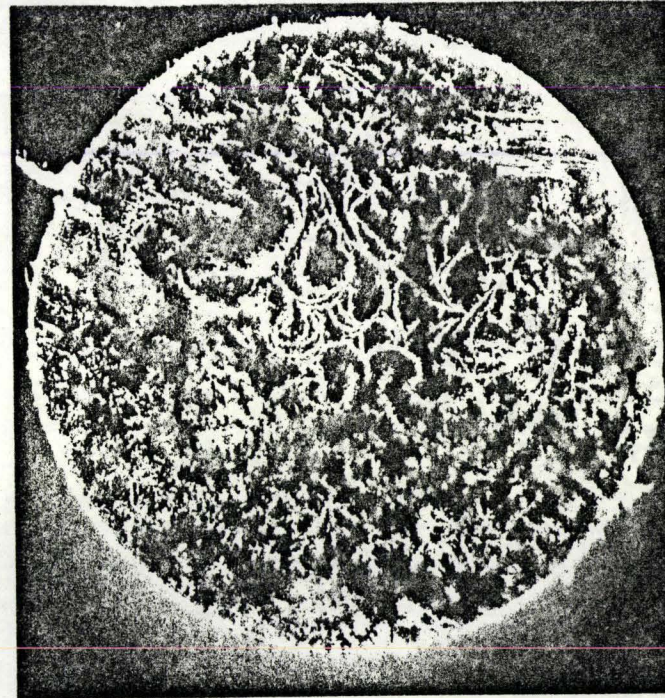
Li - implanted Ni-NiO



Sample After Polarization



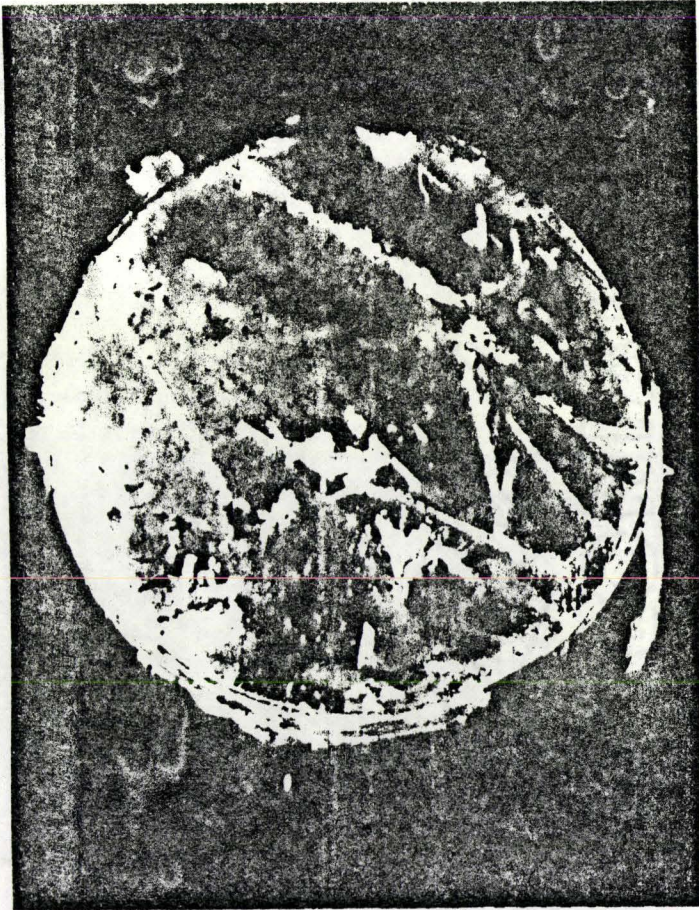
Ni electrode



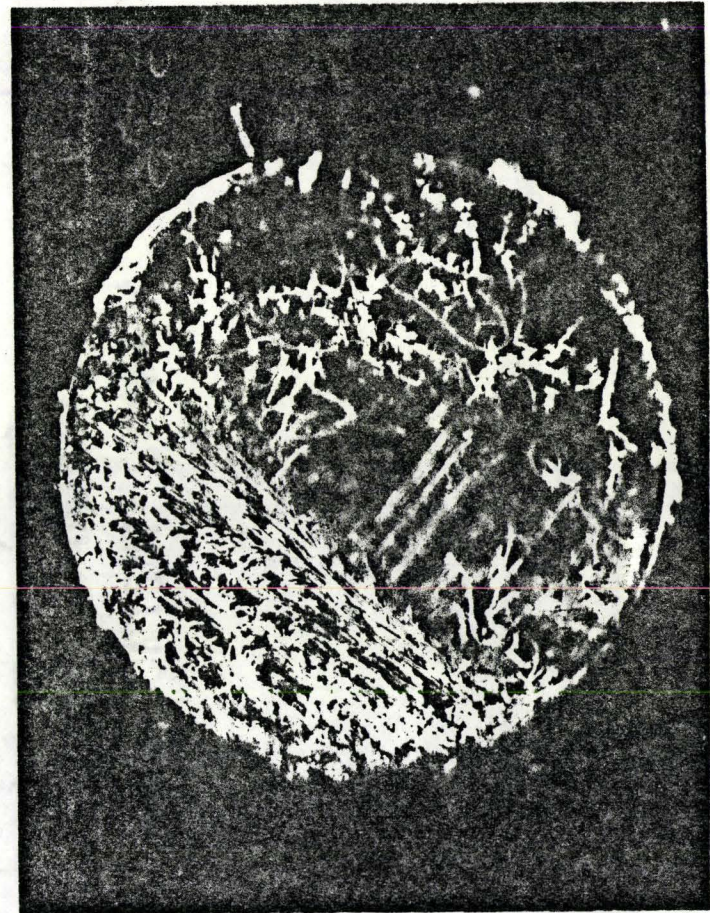
He implanted Ni electrode

FIG. 14(b)

Figure 14(b): Optical micrographs of un-implanted and implanted electrodes after Polarization.



Ni



Li - implanted Ni

Figure 14(c): Optical micrographs of un-implanted and implanted electrodes after Polarization.

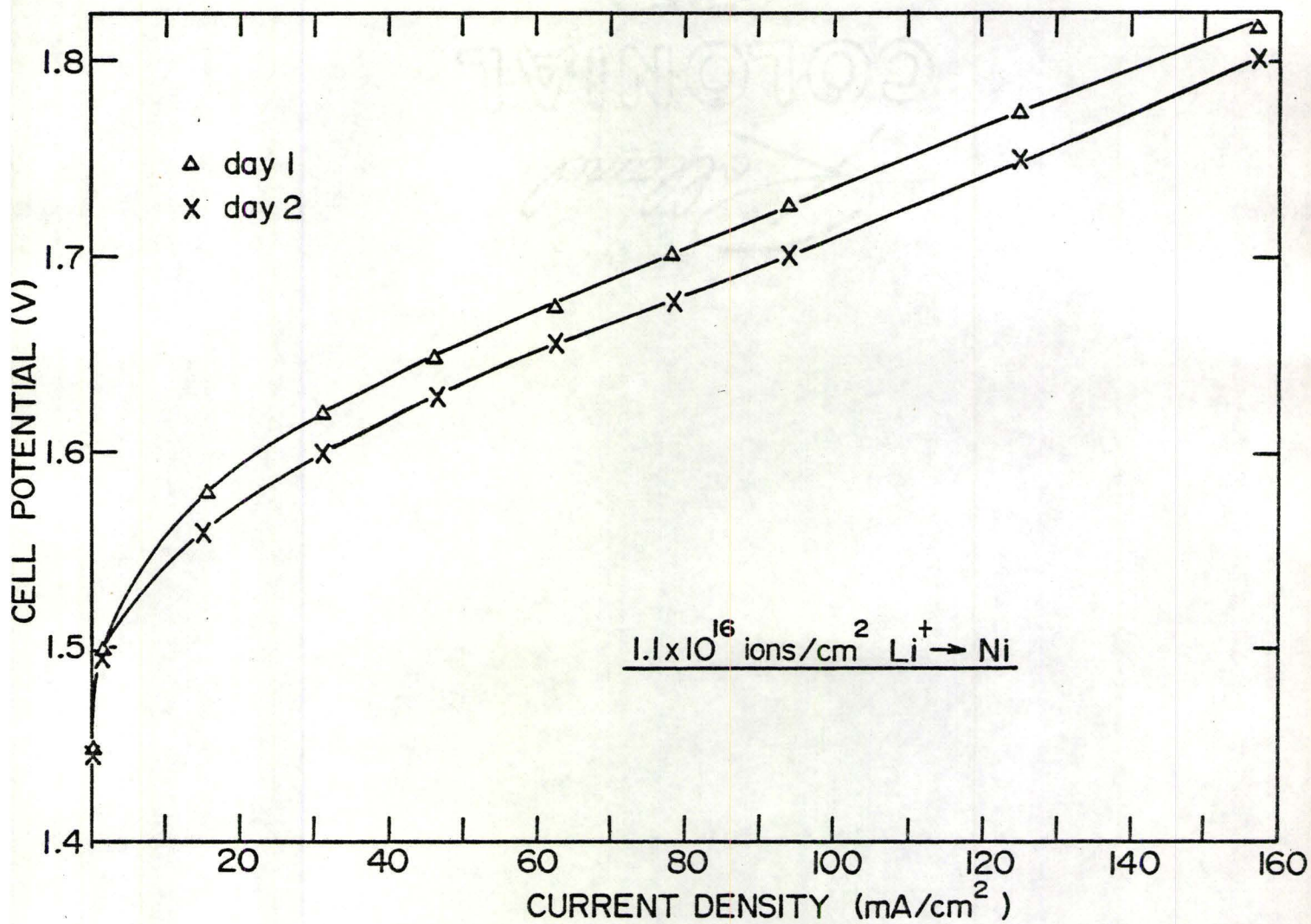


Figure 15(a): Current-potential relation for oxygen evolution on Li-implanted Ni electrode (low current density).

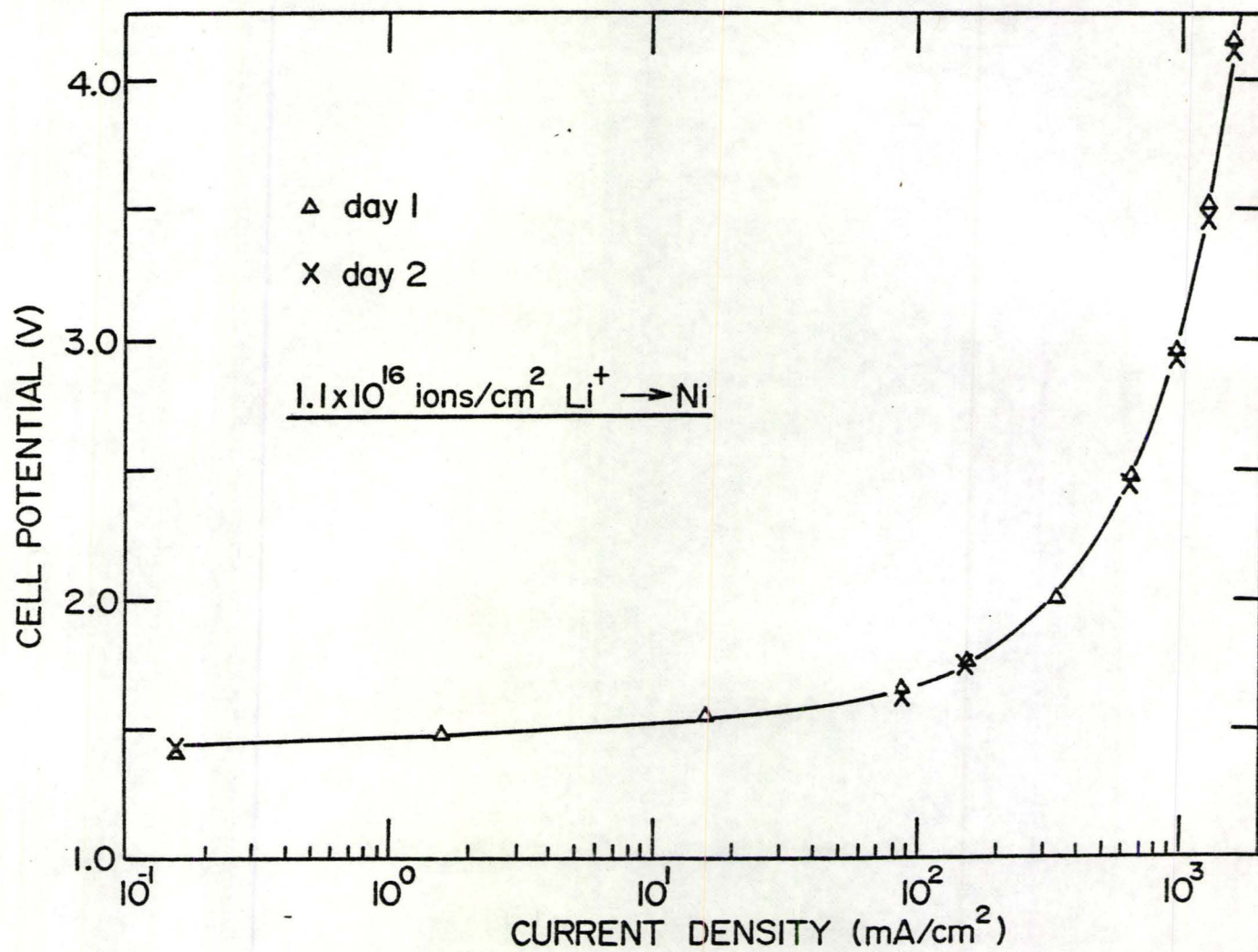


Figure 15(b): Oxygen electrode potential vs. log of current density on Li-implanted Ni (high current density).



Li - Implanted Ni (1×10^{16} atoms/cm²)

Figure 16(a): Optical micrograph of Li-implanted electrode after polarization.



Figure 16(b): Optical micrograph of Li-implanted electrode.

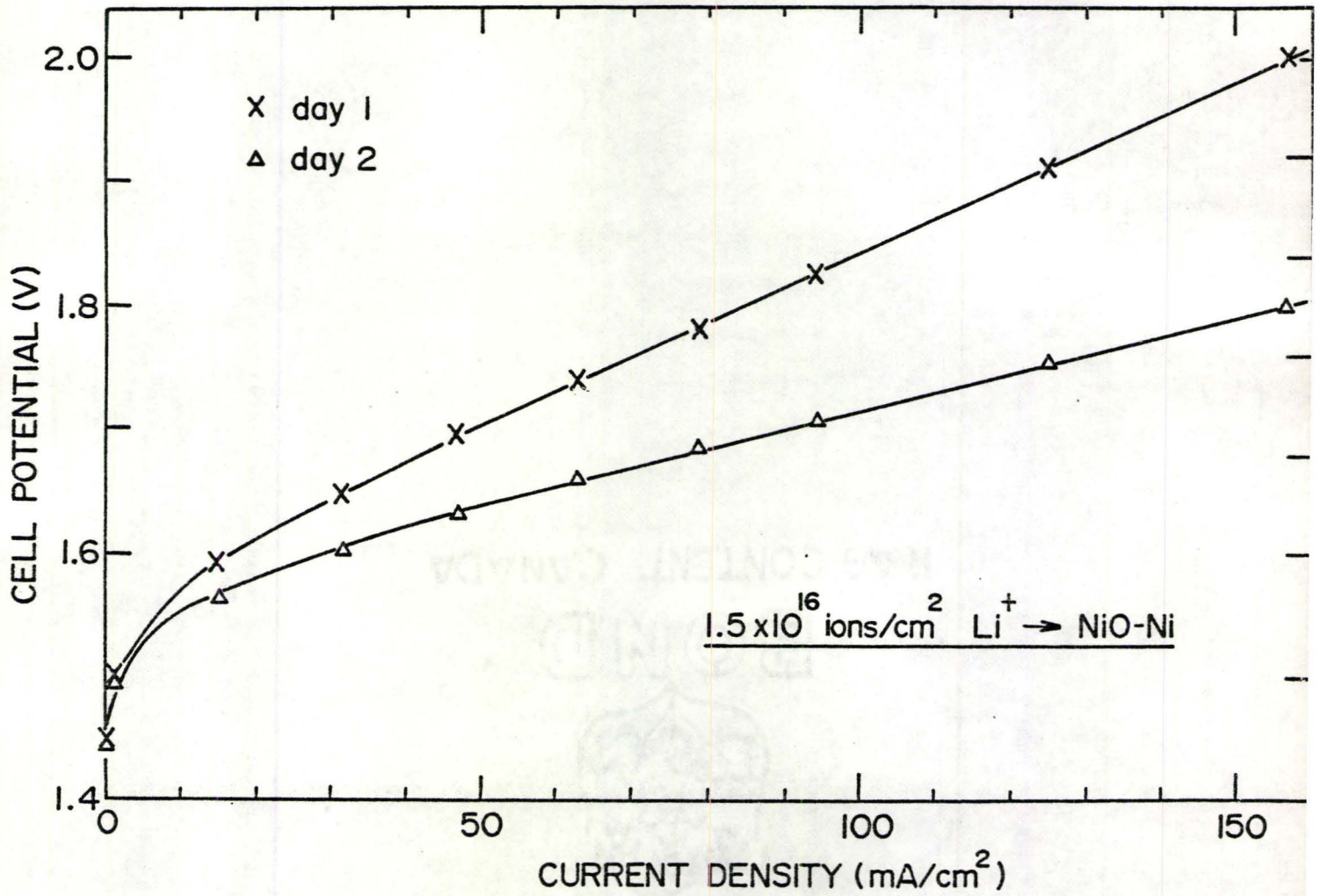


Figure 17(a): Oxygen electrode potential current density on Li-implanted NiO (low current density).

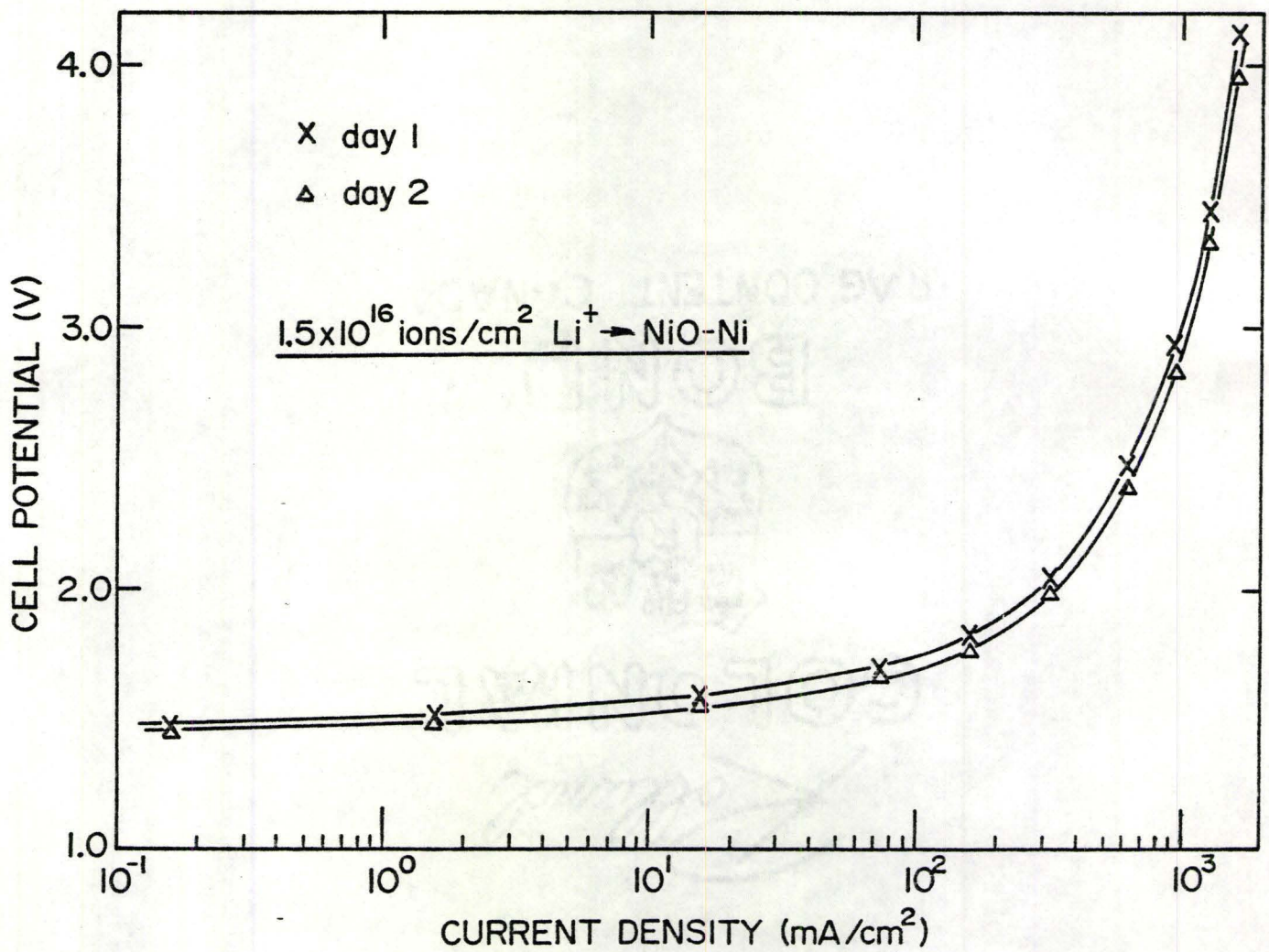


Figure 17(b): Oxygen electrode potential vs. log of current density on Li-implanted NiO electrode (high current density).

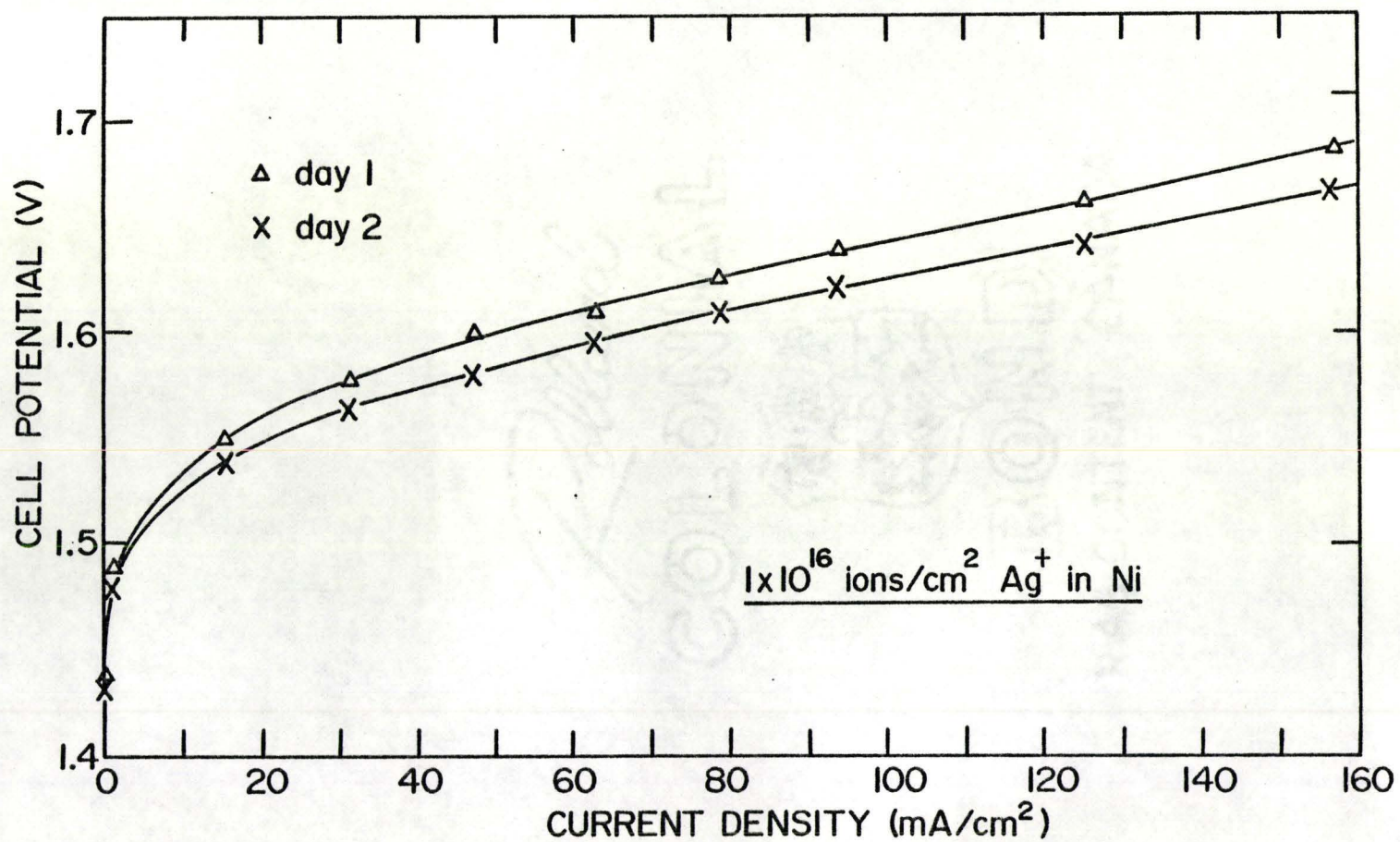


Figure 18(a): Oxygen electrode potential vs. current density on Ni into which Ag has been directly implanted (Low current density).

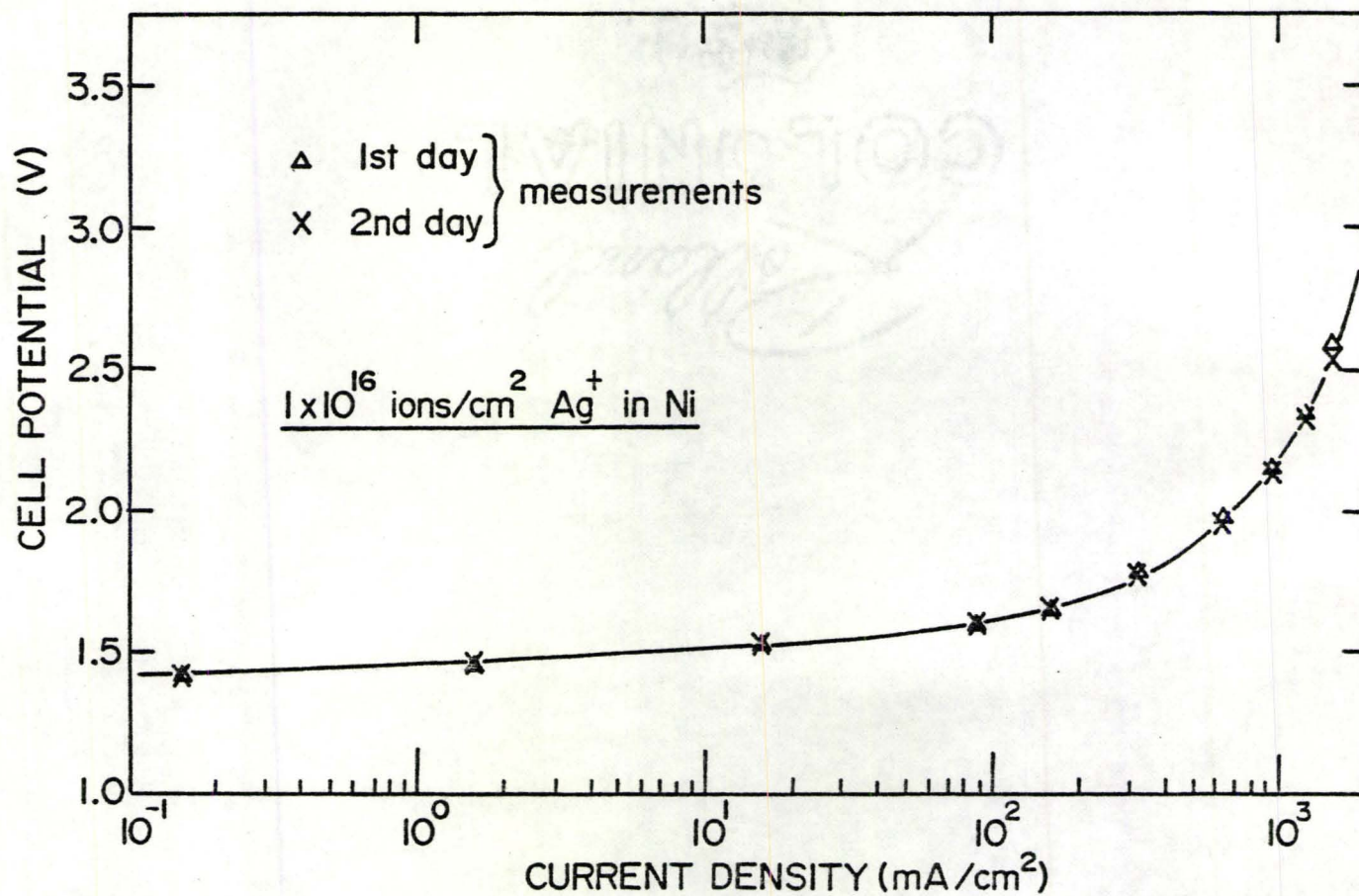


Figure 18(b): Oxygen electrode potential vs. log of current density on Ag-implanted Ni electrode (high current density).

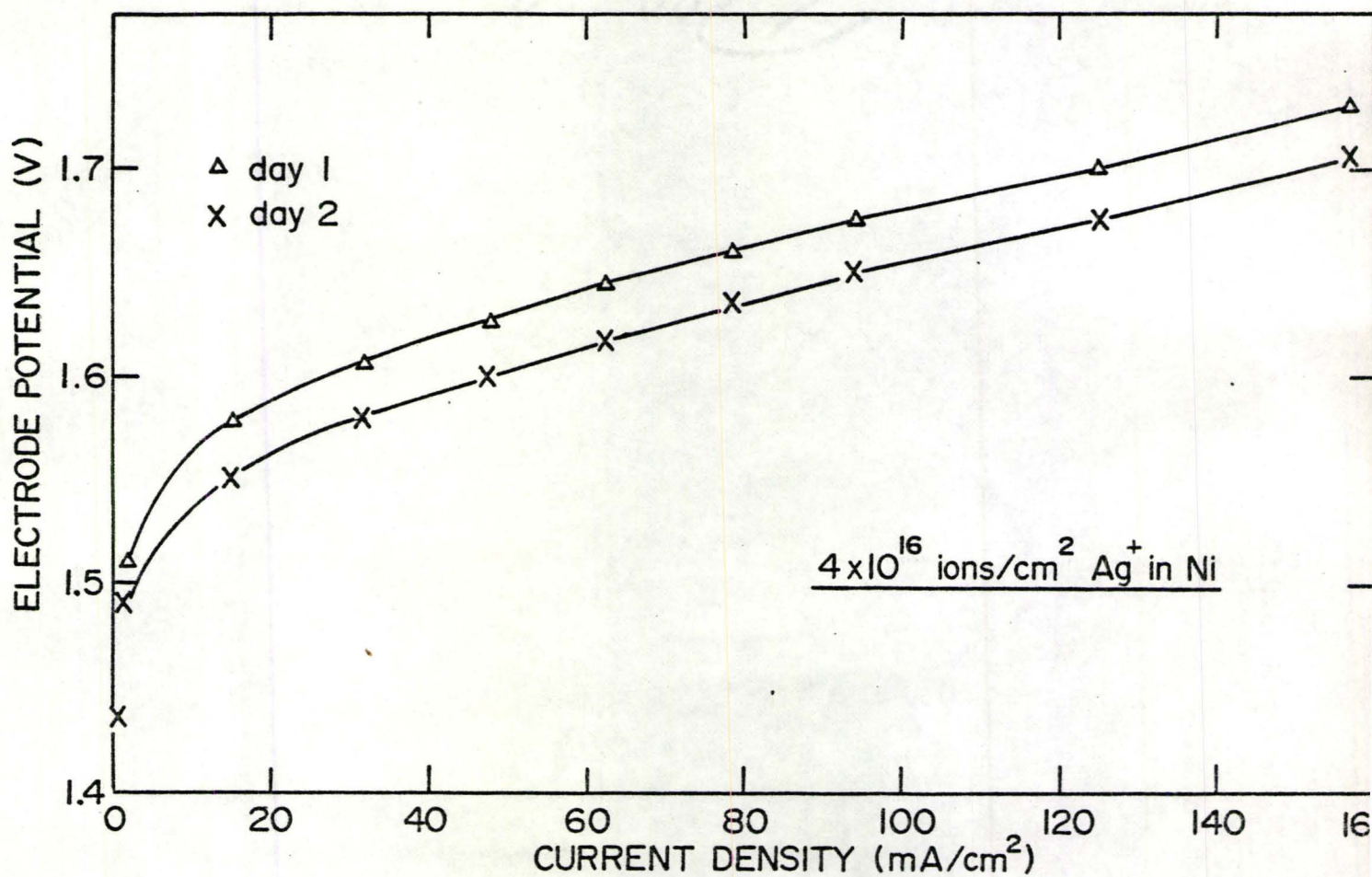


Figure 19 (a-i): Oxygen electrode potential vs. current density on Ag-implanted Ni electrode (low current density).

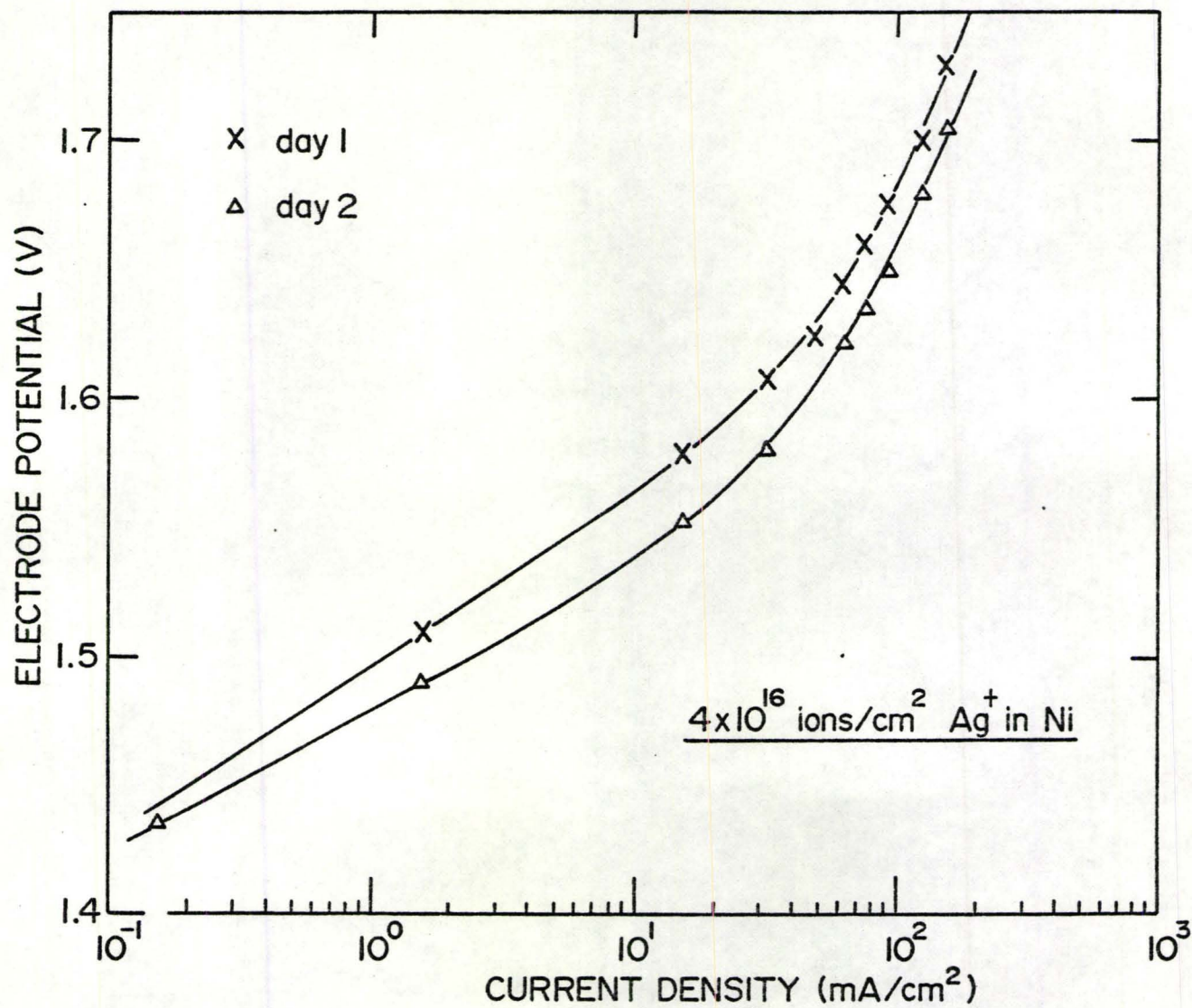


Figure 19(a-ii): Oxygen electrode potential vs. log of current density on Ag-implanted Ni electrode (low current density).

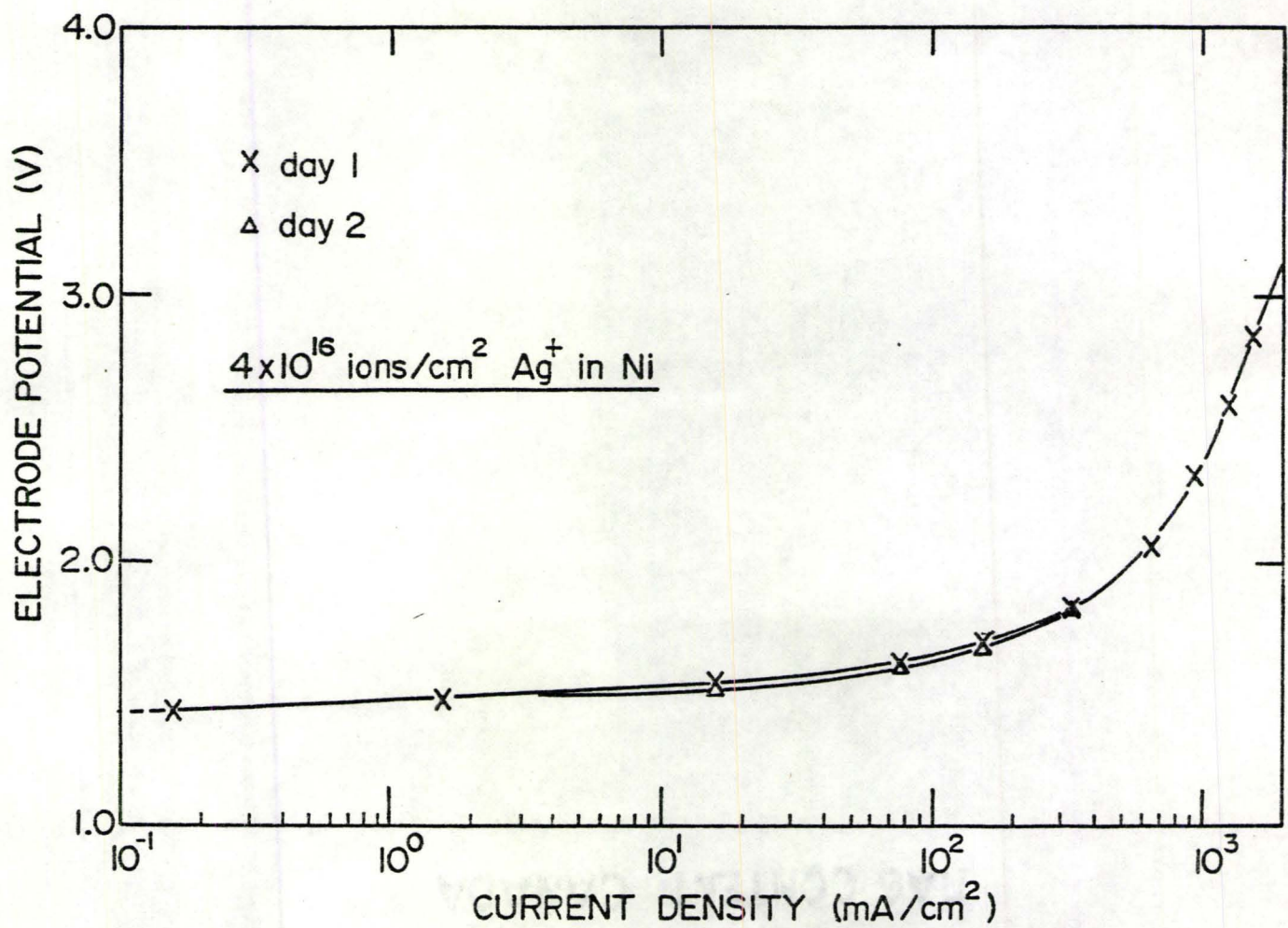
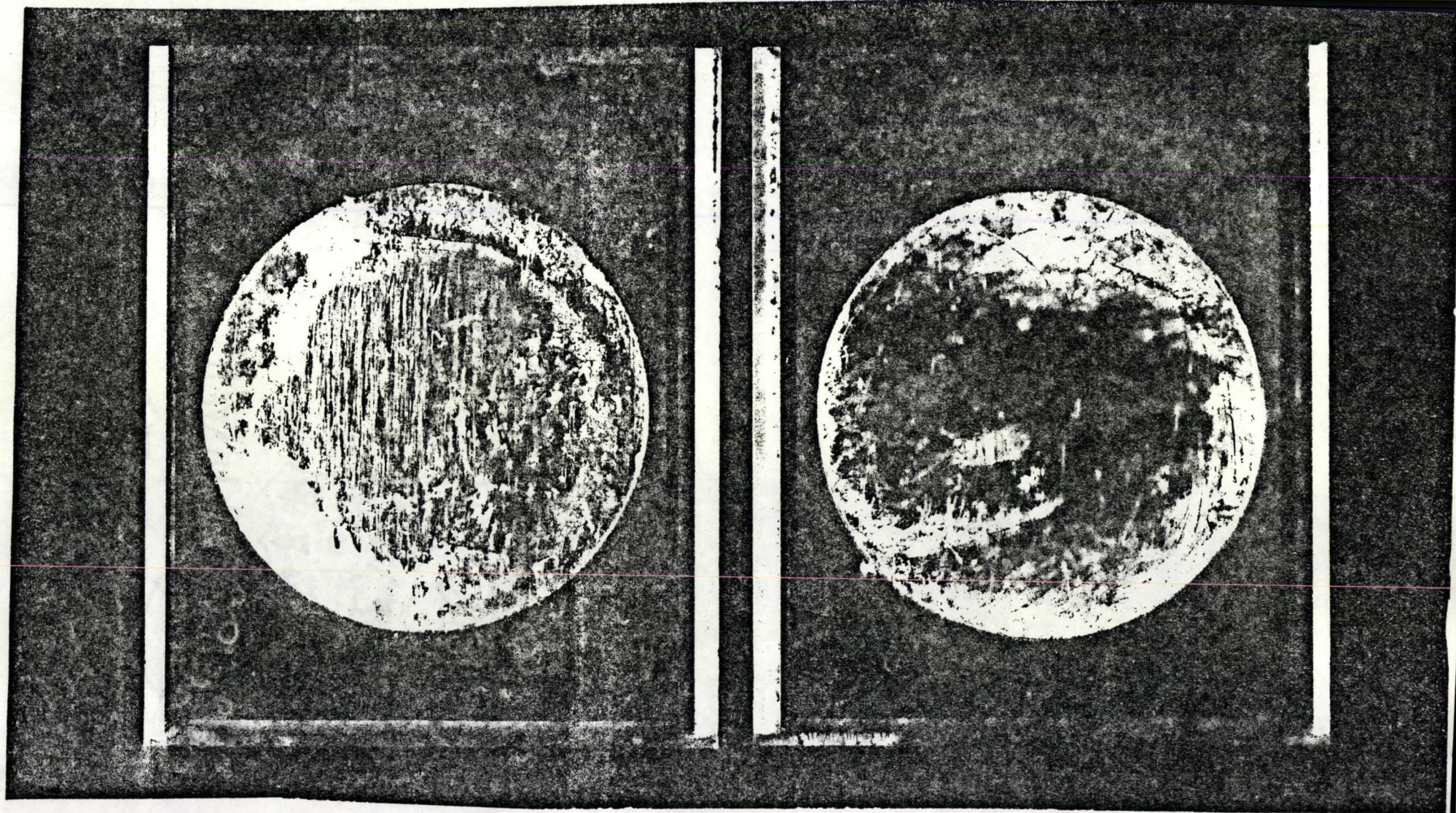


Figure 19(b): Oxygen evolution potential on Ni electrode implanted with Ag vs. log of current density (high current density).



(A)

(B)

Figure 20: Optical micrograph of Ag-implanted electrodes (a) 4×10^{16} Ag atoms/cm².
(b) 1×10^{16} Ag atoms/cm².

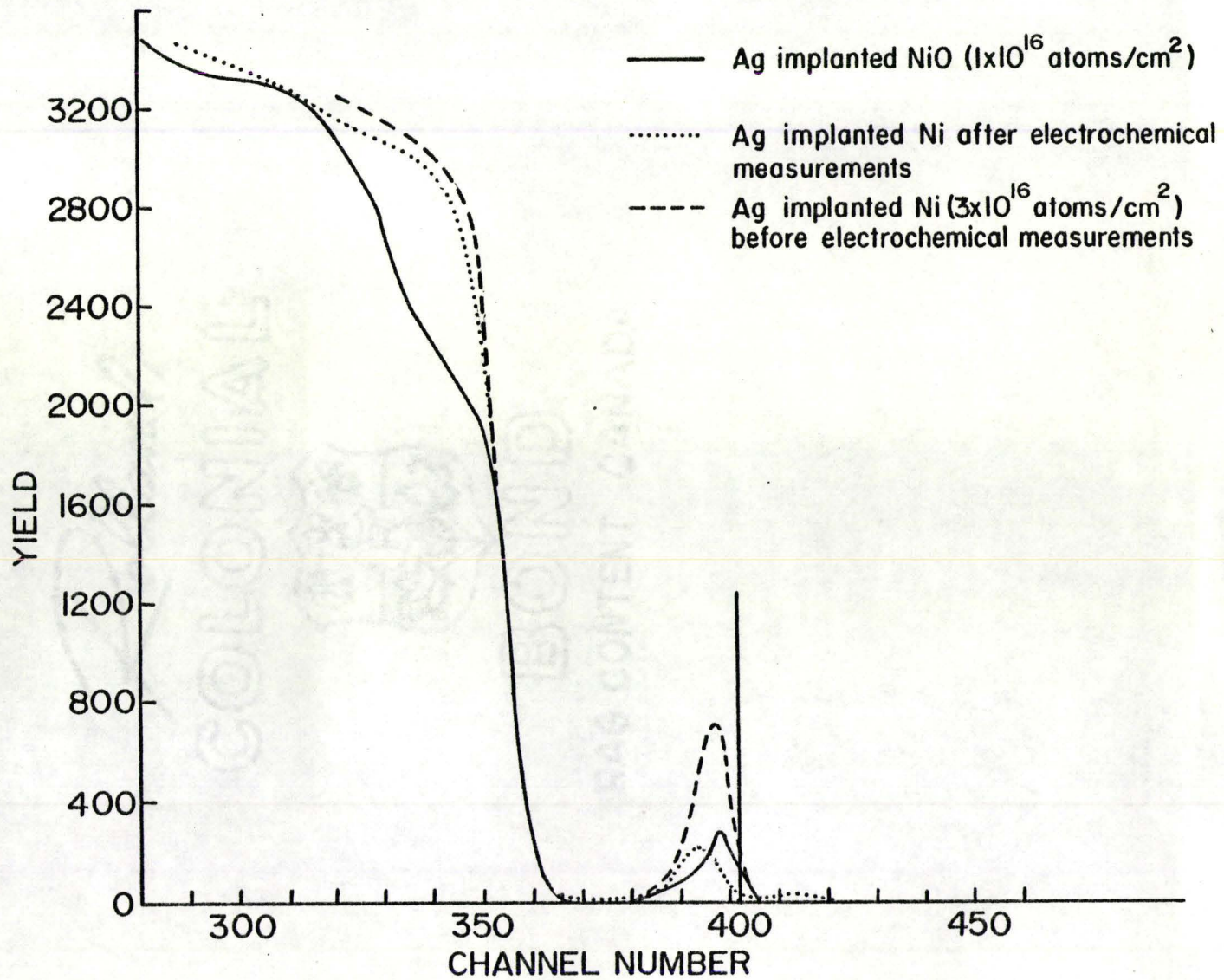


Fig. 20(c): Backscattering spectra from Ag-implanted Electrodes.

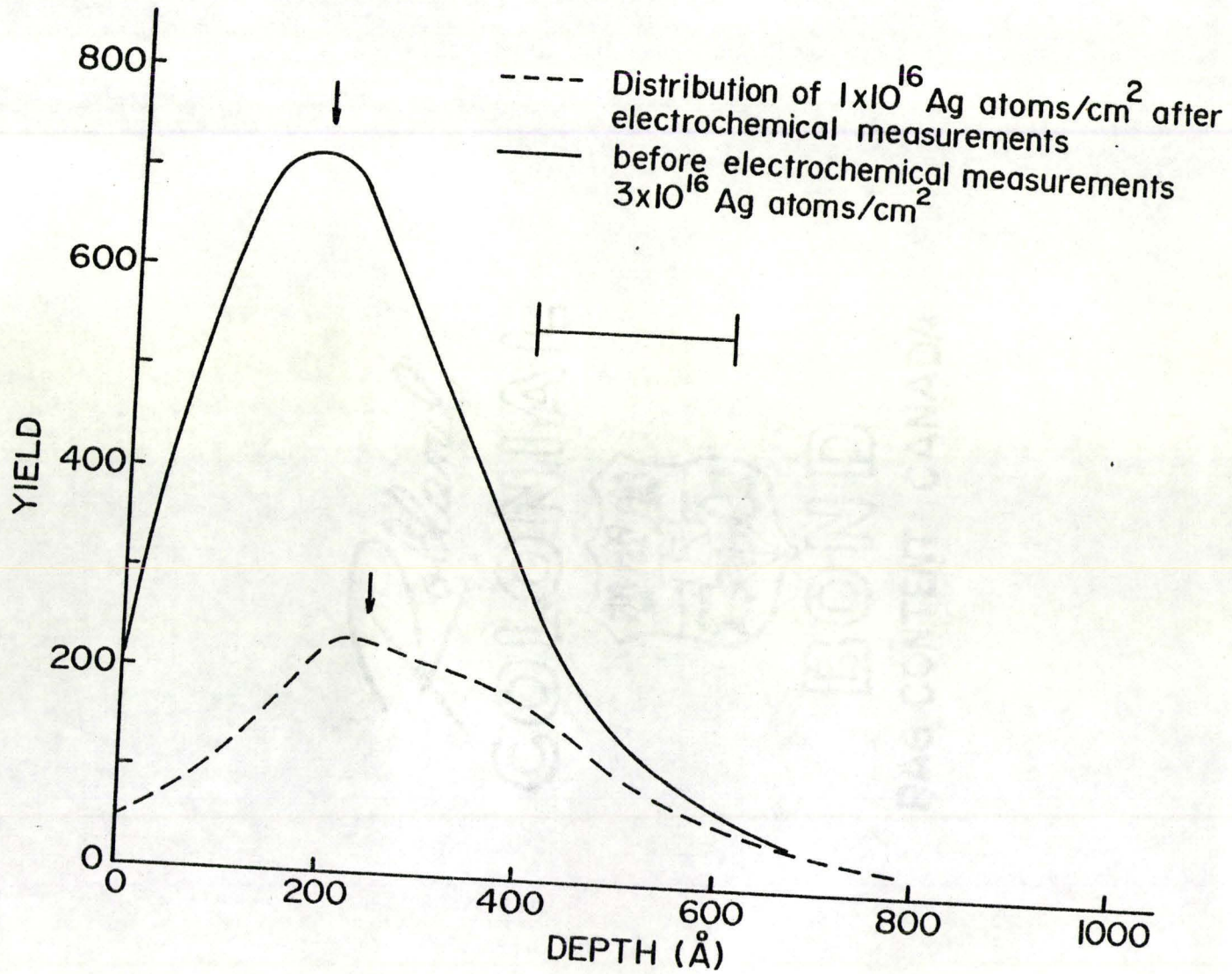


Fig. 20(d): Depth distribution of Ag in implanted electrodes.

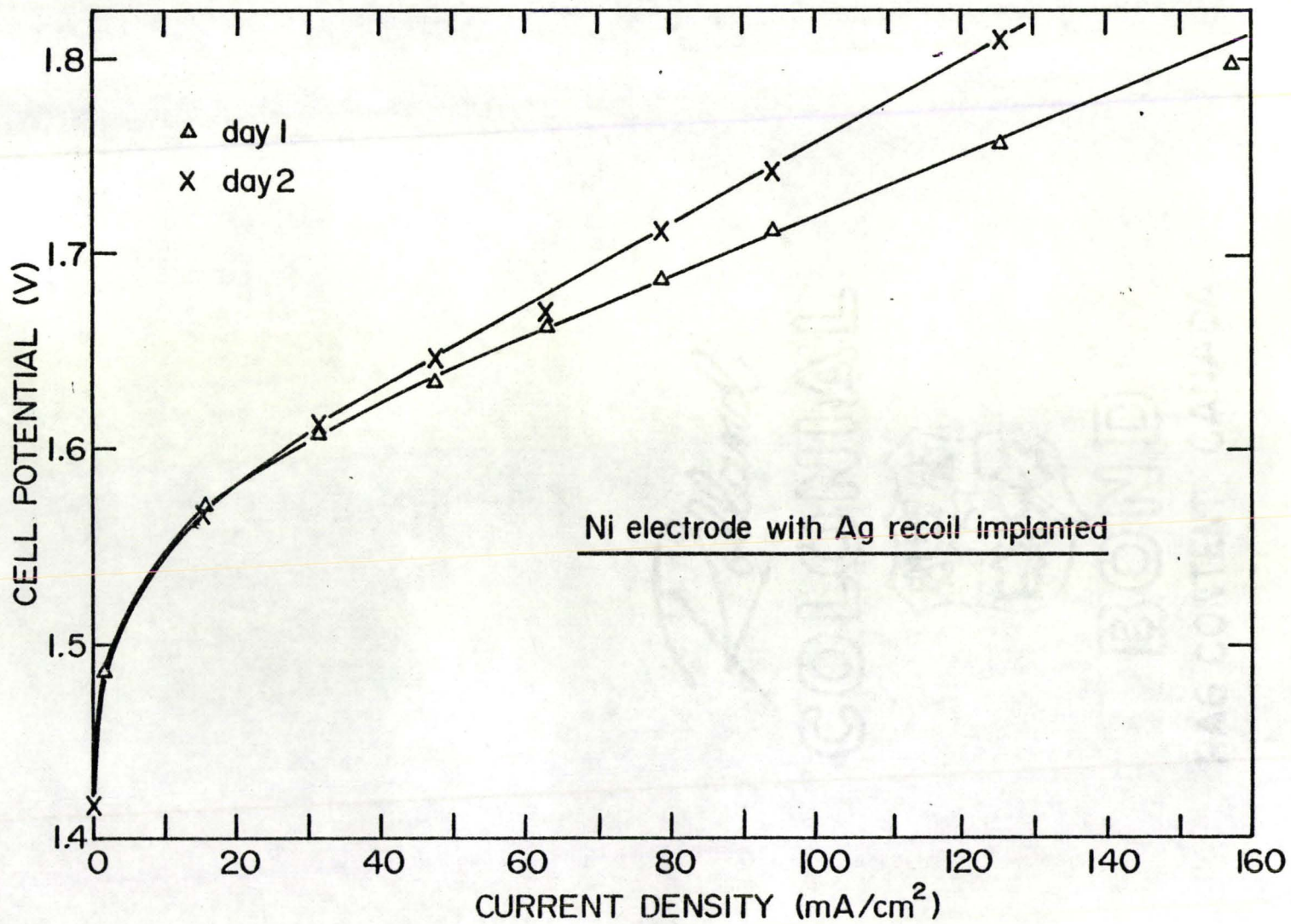


Fig. 21(a): Oxygen electrode potential vs. log of current density (low current density).

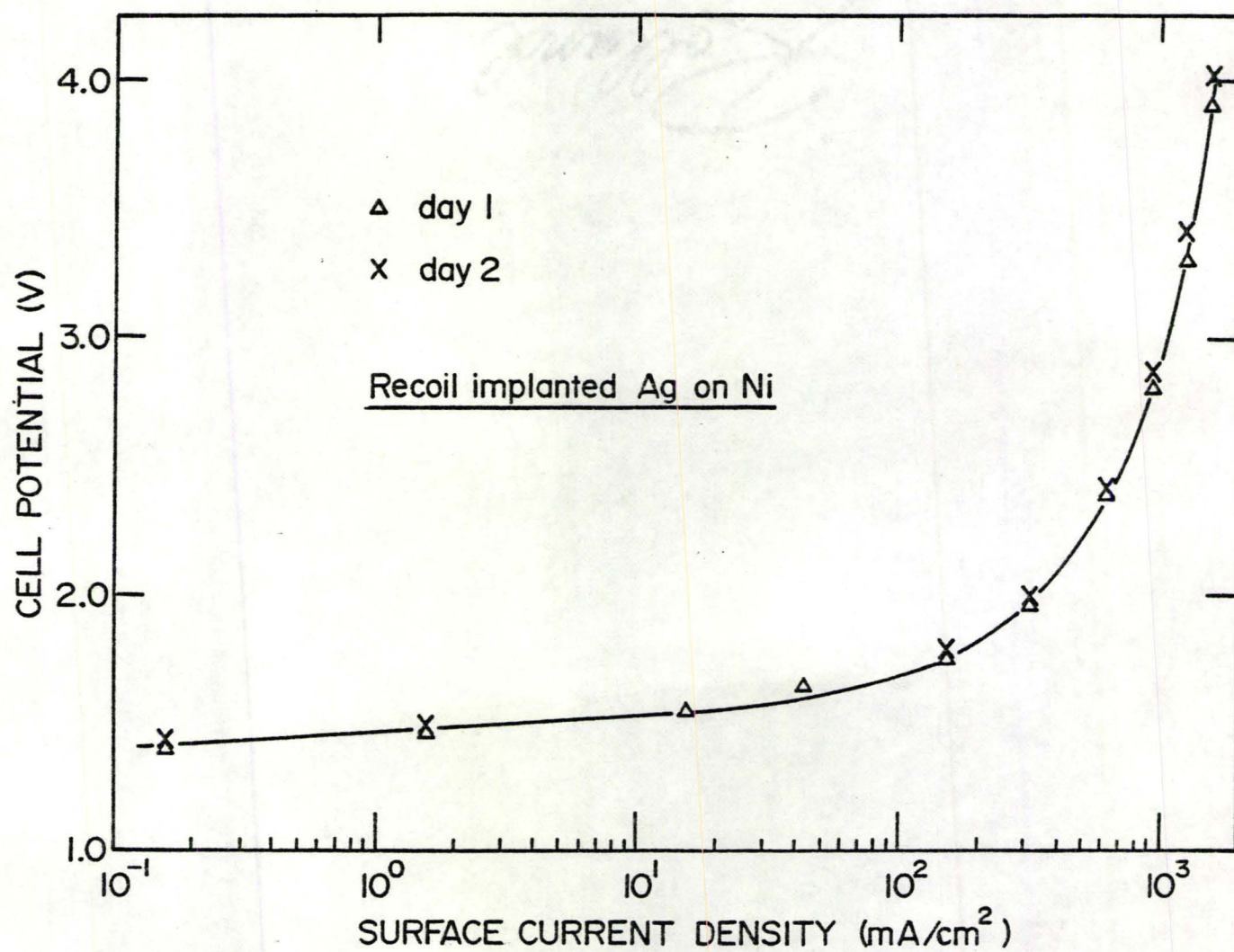


Figure 21(b): Oxygen electrode potential vs. log of current density (high current density).

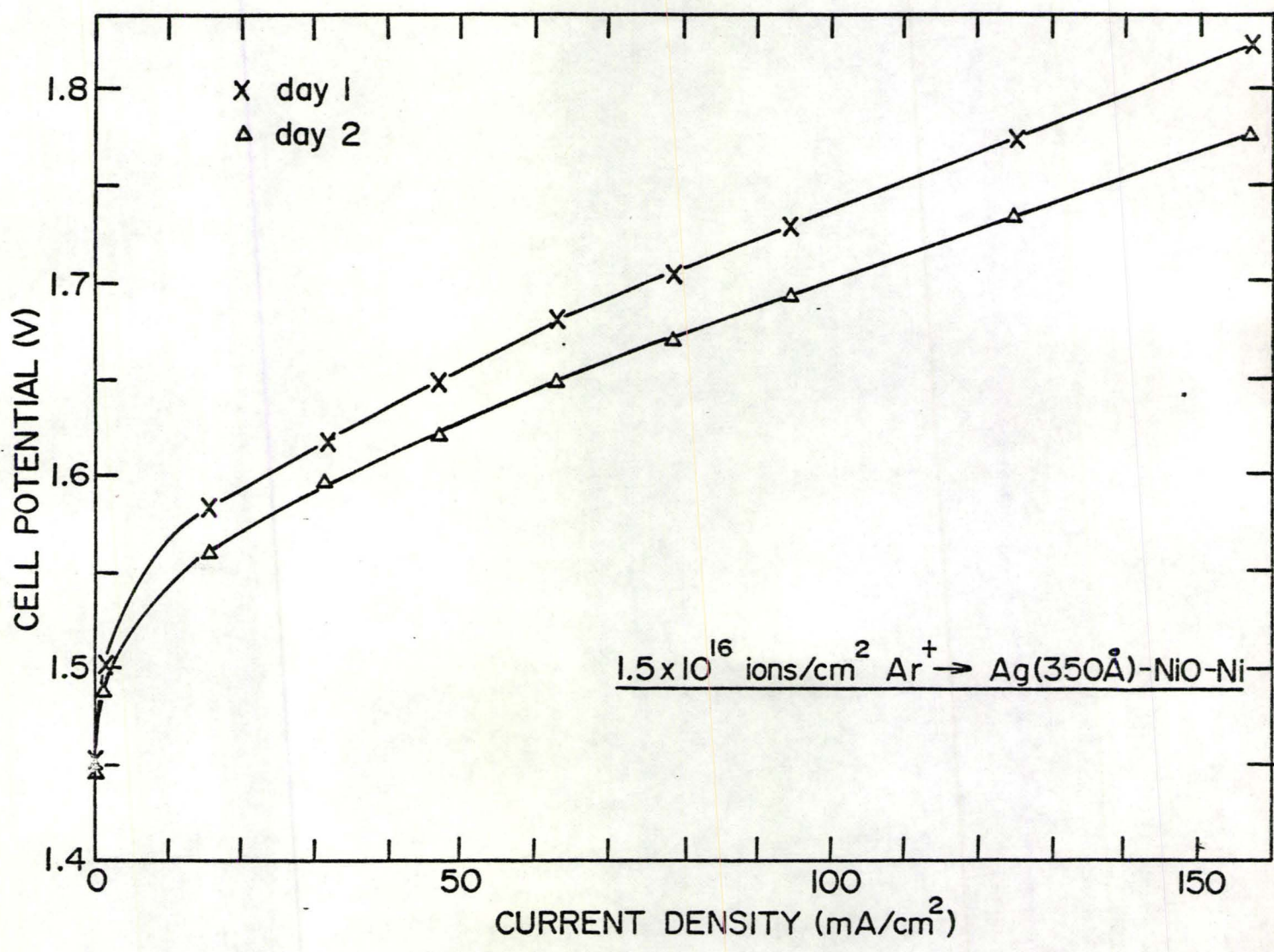


Figure 22(a): Current potential relation for oxygen evolution on NiO oxide electrode in which Ag has been recoil implanted (low current density).

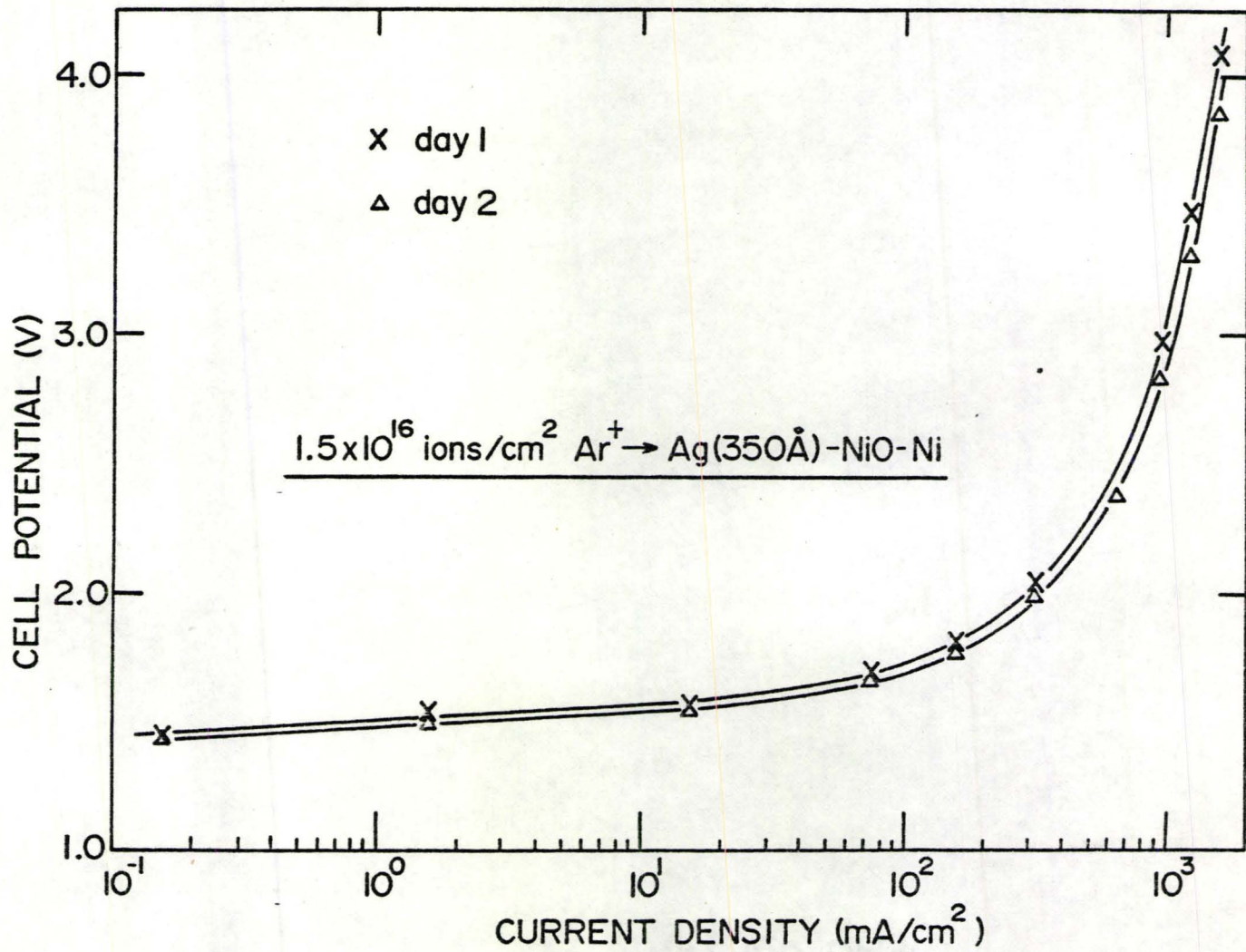


Figure 22 (b): Current-potential curve for NiO electrode recoil implanted with Ag (high current density).

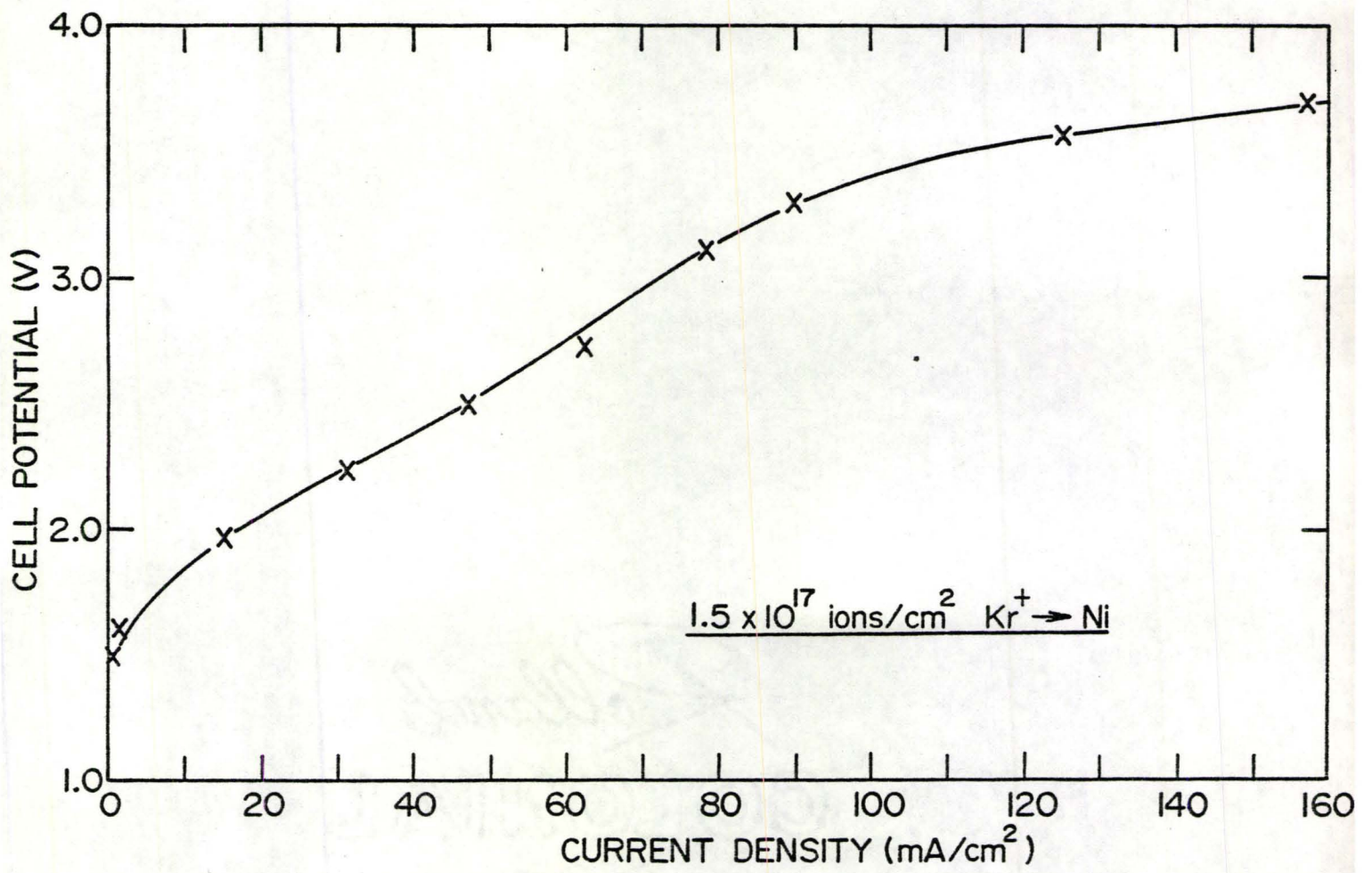


Figure 23: Current potential curve obtained for Kr-implanted Ni electrode.

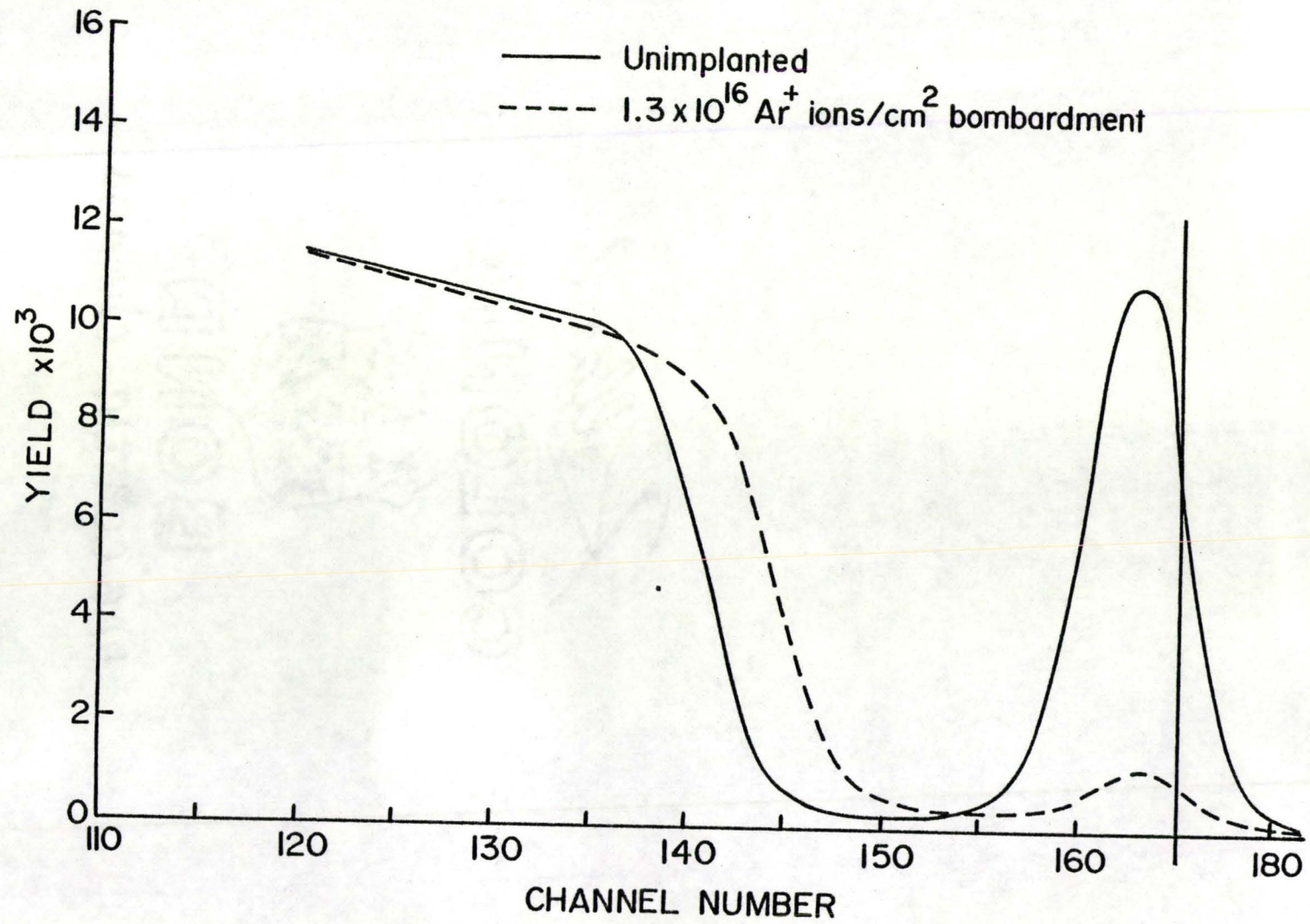


Fig. 24: RBS Spectra from Ni recoil-implanted with Ag.

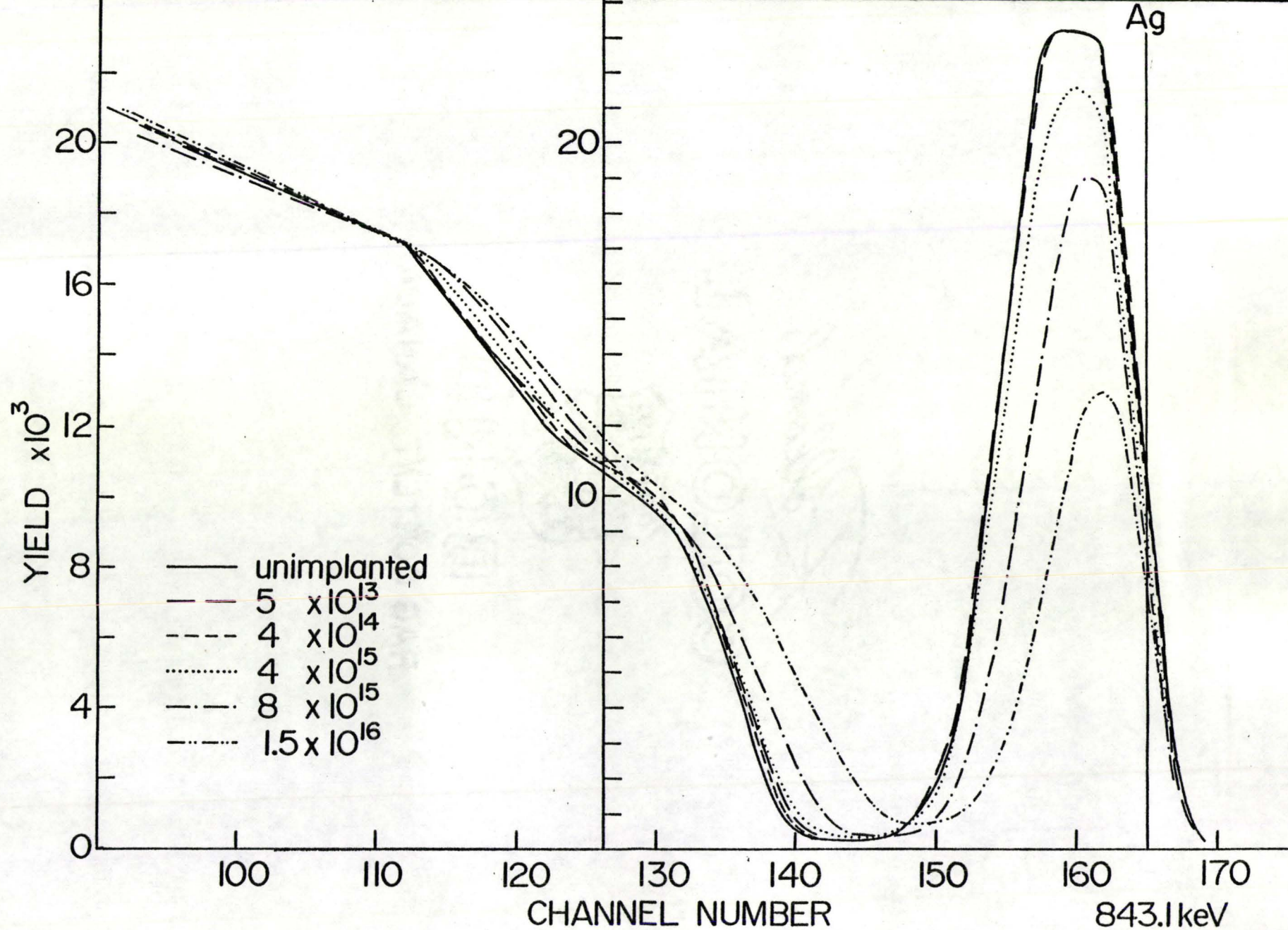


Figure 25: RBS of recoil-implanted (Ag) nickel oxide.

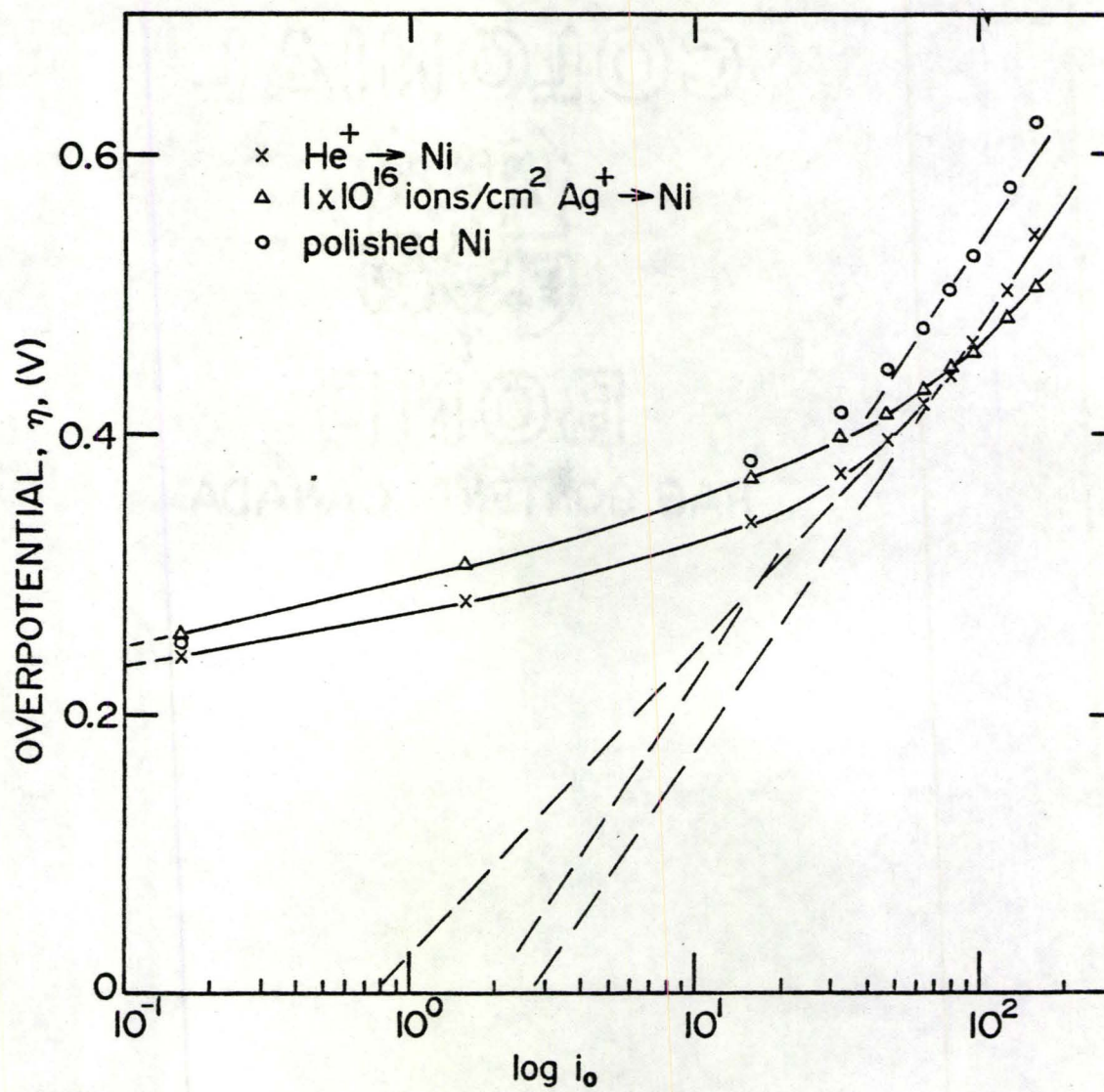


Figure 26(a): Oxygen overpotential on various electrodes vs. log of current density (low current density).

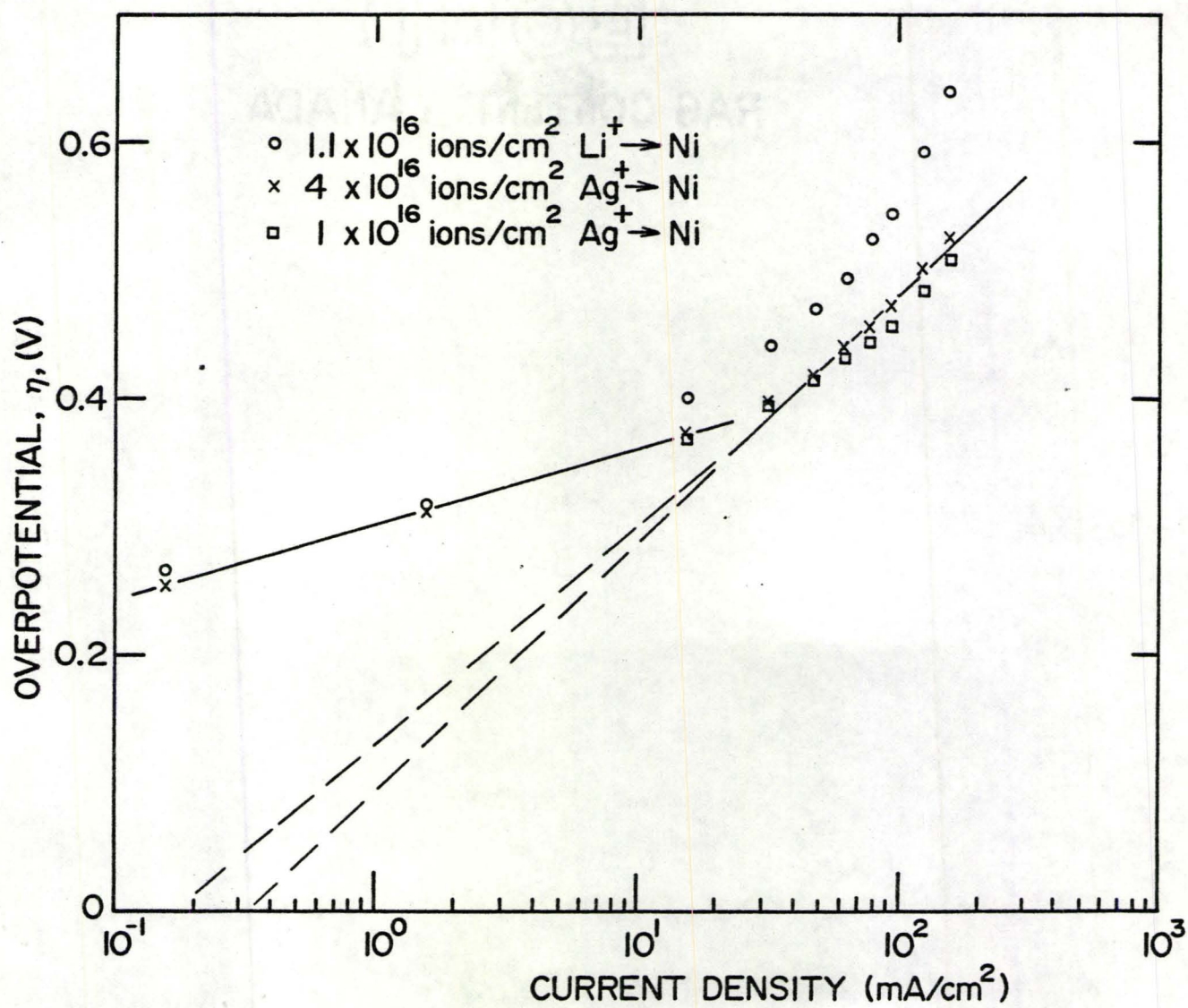


Figure 26(b): Overpotential vs. log of current density (low current density).

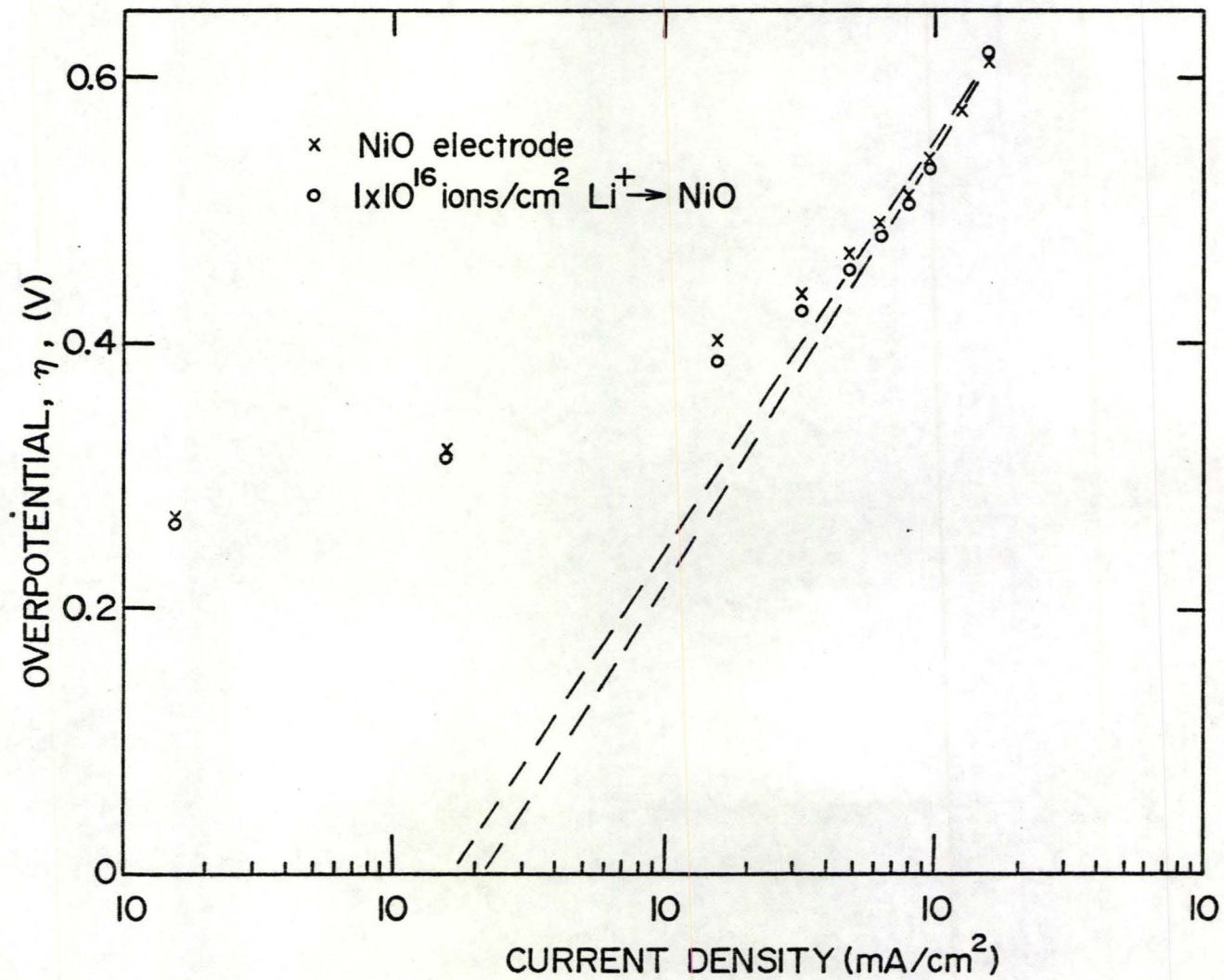


Figure 26(c): Oxygen overpotential on NiO and Li-implanted NiO vs. log of current density (low current density).

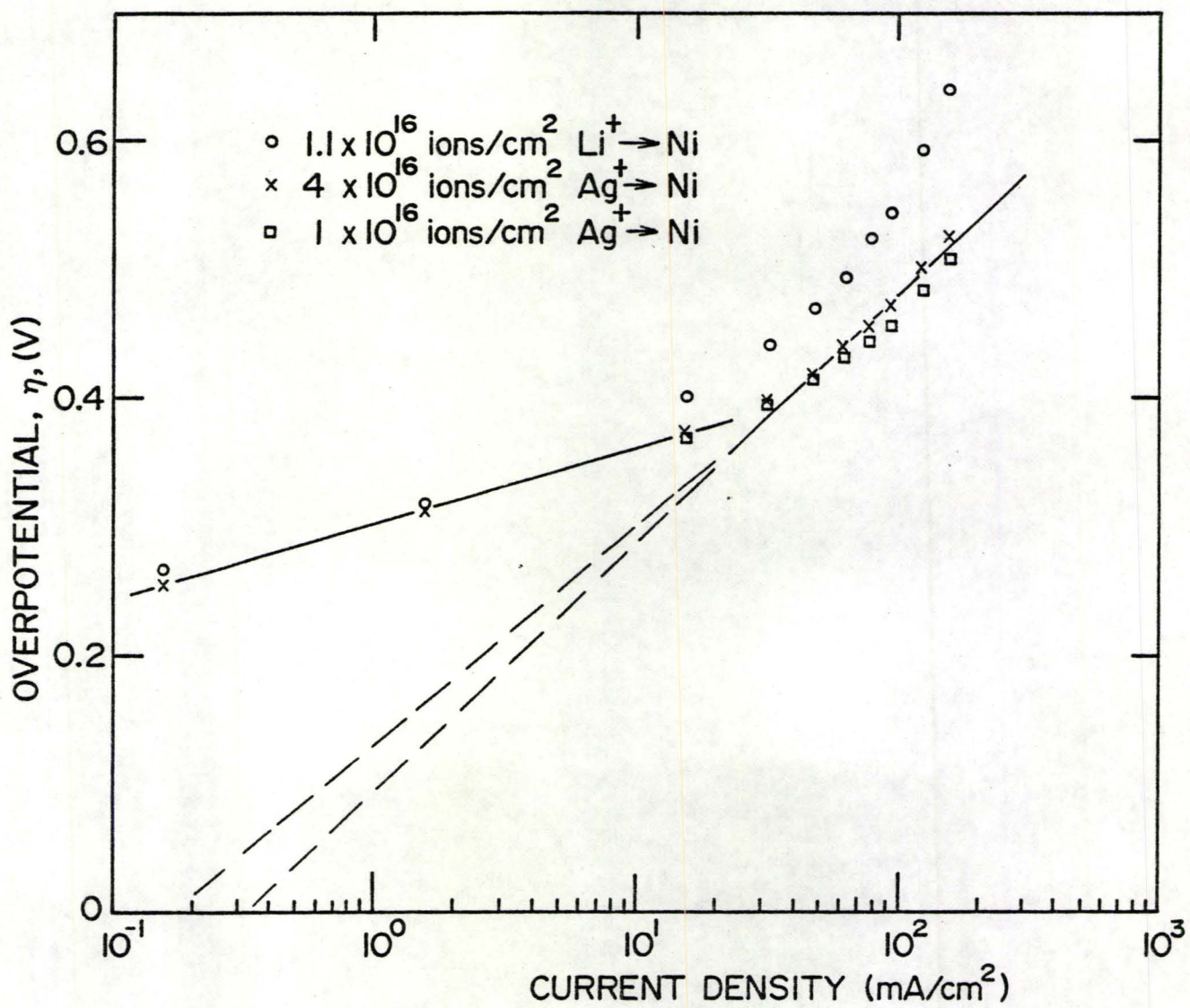


Figure 26(d): Oxygen overpotential vs. log of current density for implanted Ni electrodes (low current density).

REFERENCES

1. Lee, T.S., J. Electrochem. Soc., Vol. 118, No. 8, (Aug. 1971.) pp128
2. Miles, M.H., Kissel, G., Lu, P.W., Srinivasan, S., J. of Electrochem. Soc., Vol. 123, No. 3, (March 1976) pp. 332-326.
- 30 3. Rabette, P., Deane, A.M., Tench, A.J., Che, M., Chemical Physics Letters, Vol. 60, No. 2. (1979) pp. 348.
- 39 4. Tseung, A.C.C., Hobbs, B.S. and Tantram, A.D.S., Electrochimica Acta, 1970, Vol. 15. pp. 478-481.
5. Iwakura, C., Fukuda, K., Tamura, H., Electrochimica Acta, Vol. 21. (1976) 501
6. Iwakura, Chiaki, Kazuhiro Hirao and Hideo Tamura, Electrochimica Acta 1977 Vol. 22, pg. 335-340.
7. Miles, M.H., Huang, Y.H., J. Electrochem. Soc. Vol. 125, No. 12, (1978) 1931.
- 68 8. Tseung, A.C.C., Bevan, H.L., J. of Material Science 5 (1970), p. 604-610.
9. Martin Hammerli, AECL, Chalk River, Private Communication.
10. Grenness, M., Thompson, W.W., J. Applied Electrochemistry 4 (1974), p. 211-218.
11. Dearnaley, G., Hartley, N.E.W., "Ion Implantation of Metals and Carbides" presented at the Int. Conf. on Metallurgical Coatings, San Francisco, April, 1978.
12. Lindhard, J., Scharff, M., Phys. Rev. 124 (1961), 128.
13. Winterbon, K.B., "Range-Energy Data for KeV Ions in Amorphous Materials", published by Chalk River Nuclear Labs, Chalk River, Ont., (1968.) pp. 1-37
14. Fastrup, B., Hvelplund, P., Phys. Rev. 165 (1965).
15. Firsov, O.B., Sov. Phys. JETP 9 (1959) 1076.
16. Cheshire, L., Dearnaley, G., Poate, J.M., Proc. Roy. Soc. A311 (1969) p. 47.
17. Nelson, R.S., Rad. Effects, 1969, Vol. 2, pp. 47-50.
18. Mayer, J.W., Erickson, L., Davies, J.A., "Ion Implantation in Semiconductors", Academic Press, New York (1970).

19. Morgan, D.V., Ed. "Channelling", (John Wiley and Sons 1979).
20. Ziegler, J., Ed., "New Uses of Ion Accelerators", Plenum Press, 1975.
21. Benjamin, J.D., and Dearnaley, G., Inst. Phys. Conf. Ser. No. 28, 1976, Chap. 4. pp. 140.
22. Goode, P.D., Inst. Phys. Conf. Ser. No. 28, (1976,) Chap. 4. pp. 154-159
23. Dearnaley, G., Goode, P.D., Miller, W.S., Turner, J.F., Proc. Int. Conf. on Application of Ion Beams to Metals, Albuquerque, U.S.A. 1973, pg. 415.
24. Antill, J.E., Bennett, M.J., Dearnaley, G., Fern, F.E., Goode, P.D., Turner, J.F., Proc. Int. Conf. on Application of Ion Beams to Metals, Albuquerque, U.S.A. 1973, Plenum Press, 1974, pg. 415.
25. Naguib, H.M., Kriegler, R.J., Davies, J.A., Mitchell, J.B.: J. Vac. Sci. Technol., 13 (1976), p. 396.
26. Dearnaley, G., Sood, D.K., Rad. Effects 1978, Vol. 39, pg. 157-162.
27. Grant, W.A., Inst. Phys. Conf. Ser. No. 28, 1976, Chap 4. pp. 127-139.
28. Zeigler, J.F., Chu, W.K., At. Data Nucl. Data Tables, 13 (1974), 463.
29. Davies, J.A. and MacKintosh, "Rutherford Scattering and Channelling - A useful Combination for Chemical Analysis of Surfaces" : Analytical Chemistry Vol. 41 No. 4 (1969) 26 A.
30. Graham, M. J., Cohen, M.J., Electrochemical Soc. Vol 119 No. 7 (1972) pp. 879-883.
31. Allen R. M. : Electronics Letters Vol. 5 No. 6 (1969) pp. 111.
32. Kelly, R., Institute of Mat. Research, McMaster University, Hamilton, Ontario, Canada: Private Communication.

2.2 Recoil Implantation

Recoil implantation is the introduction of impurity atoms into a substrate by atomic recoil of atoms sitting on a target. In deliberate recoil implantation a thin layer of the material to be recoil implanted is evaporated on to a substrate (into which the implant is desired), Fig. 3. The evaporated layer and the substrate then form a composite target. The target is then bombarded with energetic ions - usually inert gas ions like Ar or Kr. In the "thin" film treatment, film thickness, bombarding ion and its energy is normally chosen so that the bombarding ion has a range greater than the film thickness. If the energy transferred to an atom in the evaporated film is greater than $E_d \sim 25$ eV (the energy required to successfully displace an atom from its lattice position) the atom is likely to be displaced from its original position thus creating a vacancy - interstitial pair (or point defects). If the energy transferred is $\gg 25$ eV, the primary displaced atom may in turn displace other atoms within the layer thus giving rise to collision cascades.

Recoil implantation can be viewed as a form of "forward sputtering" while the opposite effect, the erosion of a target surface, can be viewed as "backward sputtering". In the process of recoil implantation erosion of the evaporated layer due to sputtering is going on as well and is in fact more rapid than the rate of recoil implantation since the sputtering ratio - the number of atoms ejected from the surface per incident ion (for most ion-target combinations) is greater than unity whereas the recoil yield is often